SIMULATION BENCHMARKING AND EQUIPMENT CHARACTERIZATION FOR THE ULTRACOLD NEUTRON FACILITY AT TRIUMF

By

Beryl Rose Bell

In Partial Fulfillment
of the Requirements for the Degree
Master of Science in the
Department of Physics

McGill University, Montreal

April 2020

The way to find a needle in a haystack is to sit down.

Beryl Markham

ACKNOWLEDGEMENTS

I want to acknowledge the work and support of my colleagues and advisors which has enabled the writing of this thesis. I especially appreciate the support of my advisors Beatrice Franke and Thomas Brunner throughout the coursework, data collection, and analysis that went into this degree. Additionally all of the hours of work done by all members of the TUCAN collaboration to run the experiment during fall of 2018 were essential to the collection of the data used in this thesis. Pietro Giampa provided significant insights into the detector physics and analysis of relative response. Sean Vanbergen provided consistent wisdom and support throughout my time at TRIUMF. Wolfgang Schreyer has provided amazingly responsive troubleshooting of the simulation software. Ryohei Matsumiya has been a great resource for understanding the behaviors of the RCNP source and spectrum experiment. I also have to thank my partner Elydah Joyce, as well as my family and friends for the undying support and love throughout this process.

TABLE OF CONTENTS

LIST OF TABLES

LIST OF FIGURES

Abstract

This thesis addresses a collection of analyses and simulations done on behalf of the TRIUMF UltraCold Advanced Neutron (TUCAN) collaboration in order to contribute to the development of the new UltraCold Neutron (UCN) source in an effort to increase the precision on the measurement of the neutron Electric Dipole Moment (nEDM) to 10^{-27} $e$cm. Within this range a non-zero nEDM would verify physics beyond the standard model. In order to produce UCN, TUCAN combines accelerator driven spallation with a superfluid helium cryostat.

The first chapter details the physics background required to understand how the UCN source works and how the required precision for the nEDM measurement will be achieved. Additionally, it will introduce PENTrack, the Monte Carlo simulation software which has been developed specifically for UCN and nEDM simulations. The second chapter introduces the experimental setup at TRIUMF, including the proton beamline developed for this UCN source, the prototype source cryostat developed at the Research Center for Nuclear Physics (RCNP) of the University of Osaka, and the nEDM spectrometer which is still under development. Additionally, it will cover briefly the types of UCN experiments performed at TRIUMF in 2018, which are the main focus of this thesis, as well as the two types of UCN detectors and how they operate. Chapter 3 covers the analysis of the 2018 run relevant to this work. During this run the relative responses of two detectors were measured. Furthermore, the total accumulated proton beam intensity on target during the 2018 run was extracted from the data, followed by a verification of the correspondence of the Torodial Non-Intercepting Monitor (TNIM) reading with the extracted beam intensity. Chapter 4 is an introduction of a potential future experiment to be performed at the TRIUMF source in order to measure the energy spectrum of the UCN produced in the source using a gravity spectrometer. During the preparation for this experiment it was found that there were significant differences in measured and simulated storage lifetimes in the spectrometer. Reasons for this discrepancy are discussed and paths of investigation are presented. Chapter 5 concludes the above work and summarizes the results of this thesis and the work to follow.

Abstrait

Cette thèse porte sur un ensemble d'analyses et de simulations réalisées pour le compte de la collaboration TRIUMF UltraCold Advanced Neutron (TUCAN) afin de contribuer au développement de la nouvelle source de neutrons ultrafrais (UCN) dans le but d'augmenter la précision sur la mesure du moment dipolaire électrique du neutron (nEDM) à 10^{-27} $e$cm. Dans cette fourchette, un nEDM non nul permettrait de vérifier la physique au-delà du modèle standard. Afin de produire l'UCN, TUCAN combine la spallation commandée par l'accélérateur avec un cryostat à hélium superfluide.

Le premier chapitre détaille le contexte physique nécessaire pour comprendre le fonctionnement de la source UCN et comment la précision requise pour la mesure du nEDM sera atteinte. En outre, il présente PENTrack, le logiciel de simulation de Monte Carlo qui a été développé spécifiquement pour les simulations UCN et nEDM. Le deuxième chapitre présente le dispositif expérimental de TRIUMF, y compris la ligne de faisceau de protons développée pour cette source UCN, le cryostat prototype de la source développée au Centre de recherche en physique nucléaire (RCNP) de l'Université d'Osaka, et le spectromètre nEDM qui est toujours en cours de développement. En outre, elle couvrira brièvement les types d'expériences UCN réalisées à TRIUMF en 2018, qui sont l'objet principal de cette thèse, ainsi que les deux types de détecteurs UCN et leur fonctionnement. Le chapitre 3 couvre l'analyse de la série 2018 pertinente pour ce travail. Au cours de ce cycle, les efficacités relatives de deux détecteurs ont été mesurées. De plus, l'intensité totale du faisceau de protons accumulé sur la cible pendant la campagne 2018 a été extraite des données, suivie d'une vérification de la correspondance entre la lecture du moniteur torodique sans interception (TNIM) et l'intensité du faisceau extrait. Le chapitre 4 est une introduction à une future expérience potentielle à réaliser à la source TRIUMF afin de mesurer le spectre d'énergie de l'UCN produit dans la source à l'aide d'un spectromètre de gravité. Lors de la préparation de cette expérience, il a été constaté qu'il y avait des différences significatives entre les durées de vie mesurées et simulées du spectromètre. Les raisons de cette différence sont discutées et des pistes de recherche sont présen-

tées. Le chapitre 5 conclut les travaux ci-dessus et résume les résultats de cette thèse et les travaux à suivre.

Statement of Contribution

The contributions to this thesis can be described as the following. The work of the first chapter is a summary of work done towards the search for physics beyond the Standard Model, specifically of the improvement of the upper limit of the neutron electric dipole. The second chapter covers experimental developments in the search for the neutron electric dipole moment. It also details the development of the TRIUMF ultracold neutron source. Chapter 3 introduces experimental concepts and data collection which were the result of the efforts of the TUCAN collaboration. All analysis and simulations in chapter 3 were performed by me. Chapter 4 references results of data taken at the Research Center for Nuclear Physics (RCNP) in Osaka which were analyzed by Ryohei Matsumiya in his thesis. The simulations of the RCNP spectrum bottle and revisited analysis of RCNP data were conducted by me.

CHAPTER 1

ULTRACOLD NEUTRON PHYSICS AND THE TUCAN COLLABORATION

In contemporary physics the push to discover and quantify phenomena beyond the Standard Model of particle physics is at the forefront of fundamental research. Among the questions left open by the Standard Model of particle physics is an explanation for the baryon asymmetry in the universe [1]. One of the conditions for Baryon asymmetry is a violation of charge-parity (CP) symmetry, as described by Sakharov [2]. One source of this CP violation could be the existence of a neutron electric dipole moment (nEDM) [3]. Thus the measurement of the nEDM is an excellent probe for models beyond the Standard Model of particle physics [4]. Most experiments searching for a limit on this value utilize UltraCold Neutrons (UCN), which are slow moving neutrons. The low kinetic energy of these UCN allows them to be contained and stored. These UCN have been used to make precise measurements of the nEDM [5] [6] [7], as well as of the neutron lifetime [8] [9], free neutron beta decay correlations [10], and the neutron interaction with gravity [11]. Experiments refining the limit on the nEDM are being conducted across the globe, including efforts in Switzerland, France, Japan, Canada, and the USA. The content of this thesis involves work done at TRIUMF in Vancouver, Canada, where a next generation UCN source is being developed and built with the objective of proving world class UCN densities for a competitive nEDM measurement.

1.1 TUCAN collaboration

A new next generation UCN source and nEDM spectrometer is being developed as part of a Japanese-Canadian collaboration called **T**RIUMF **U**ltra **C**old **A**dvanced **N**eutron (TUCAN) collaboration. This collaboration was formed with the intention of combining the expertise of UCN source development from Japan at the Research Center for Nuclear Physics (RCNP) at the University of Osaka with the proton beamline infrastructure for spallation neutron production at TRIUMF, the Vancouver based accelerator facility. This combination of resources will allow TUCAN to fulfill its stated goals of constructing a next generation UCN source and improving the measurement precision of the search for a nEDM by an order of magnitude.

A UCN source prototype was developed, commissioned, and characterized at RCNP [12]. This prototype was shipped to TRIUMF and the source began operation there in 2017. The source has been run for about a month each year from 2017 until now. These runs, as well as extensive simulation work, have been supporting research and development activities for a new TUCAN source and nEDM experiment.

1.2 Neutron Electric Dipole Moments and CP Violation

The neutron is known to have a magnetic dipole moment, due to its composition of charged quarks moving in their bound state which composes the neutron. This magnetic dipole is well known [13]. The existence of a corresponding electric dipole moment would be determined by the internal structure of the neutron. Such a dipole is typically measured in units of of $e$cm. The existence of both the magnetic and electric dipole can be shown to cause a CP violation given a neutron in an electric ($\mathbf{E}$) and magnetic ($\mathbf{B}$) field. This violation will be detailed below.

In Fig. 1.1 the results of applying the parity (P) and time (T) reversal operators to a neutron with both an electric and magnetic dipole moment in an electric and magnetic field are visualized. Given the Charge-Parity-Time theorem, a T-violation is equivalent to a CP violation, where CP

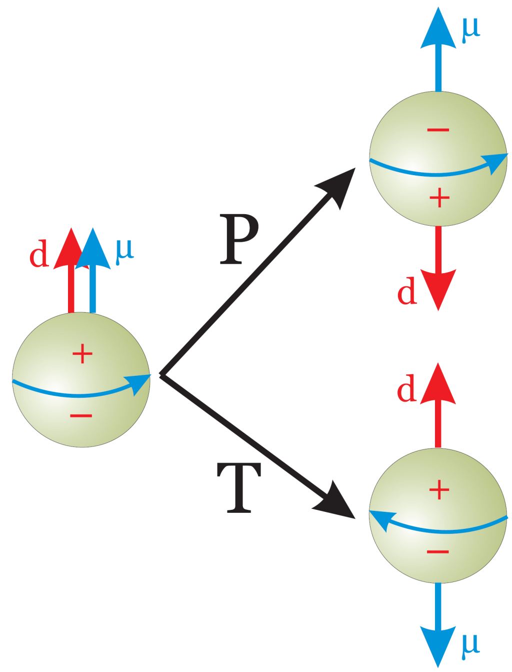

Figure 1.1: Visualization of P and T violation given a nEDM. Here the parity operator is represented by P, the time operator is represented by T. The neutron electric dipole is represented by d and the magnetic dipole is represented by μ. The breaking of symmetry in the neutron given a non-zero electric dipole can be seen under both of these operations [14].

is the combination of the charge and parity reversal operators [4]. Under time reversal the magnetic dipole moment (μ) changes direction relative to the electric dipole moment (d). This can be demonstrated with a neutral non-relativistic particle of spin ($\mathbf{S}$) in an electric ($\mathbf{E}$) and magnetic ($\mathbf{B}$) field described by the following Hamiltonian (H):

$$H = -\mu \mathbf{B} \cdot \frac{\mathbf{S}}{S} - d\mathbf{E} \cdot \frac{\mathbf{S}}{S}. \tag{1.1}$$

An application of the parity reversal operator transforms the Hamiltonian as follows:

$$\mathrm{P}(\mathbf{B} \cdot \mathbf{S}) = \mathbf{B} \cdot \mathbf{S}, \tag{1.2}$$

$$\mathrm{P}(\mathbf{E} \cdot \mathbf{S}) = -\mathbf{E} \cdot \mathbf{S}. \tag{1.3}$$

The operation in Eqn. 1.3 corresponds to the top of Fig. 1.1. In this case the reversal of parity causes the electric dipole measurement to flip, but the magnetic dipole measurement remains unchanged. This implies that if d is non-zero then there is a parity violation. Similarly, under a time reversal:

$$\mathrm{T}(\mathbf{B} \cdot \mathbf{S}) = \mathbf{B} \cdot \mathbf{S}, \tag{1.4}$$

$$\mathrm{T}(\mathbf{E} \cdot \mathbf{S}) = -\mathbf{E} \cdot \mathbf{S}. \tag{1.5}$$

The operation in Eqn. 1.5 is shown in the bottom of Fig. 1.1. Under a time reversal operation, the magnetic dipole measurement is flipped, but the electric dipole measurement is unchanged. Therefore, there is a time reversal violation. By the CPT theorem time symmetry violation is equivalent to a CP violation [4].

Within the Standard Model of particle physics the nEDM is predicted to be on the scale of 10^{-31} *e*cm [4]. This value is constrained by the limited allowed CP violation within the Standard Model, originating from the relative phases of terms within the Lagrangian of the extended theory [3]. This value is beyond a feasible measurement using the current experimental methods. However, models beyond the Standard Model predict different values for the amount of allowed CP violation, and thus different values for the nEDM. These theories can also explain baryon asymmetry [1]. For example supersymmetry (SUSY), described by a combination of string and compactified M-theories, predicts larger values for the nEDM, to a value that is within a measurable range [3].

Theories beyond the Standard Model, which require additional CP violation, can explain current discrepancies between experimental observations and theoretical predictions of the Standard Model [1]. Some of these discrepancies include the measured ratio between the baryon number density (n_{B}) and the photon number density (n_γ) of the universe. The current measured ratio is $\frac{n_{\mathrm{B}}}{n_\gamma} \approx 10^{-10}$ [15][16].

There is no proven theoretical motivation for such a large asymmetry, which is expected to be

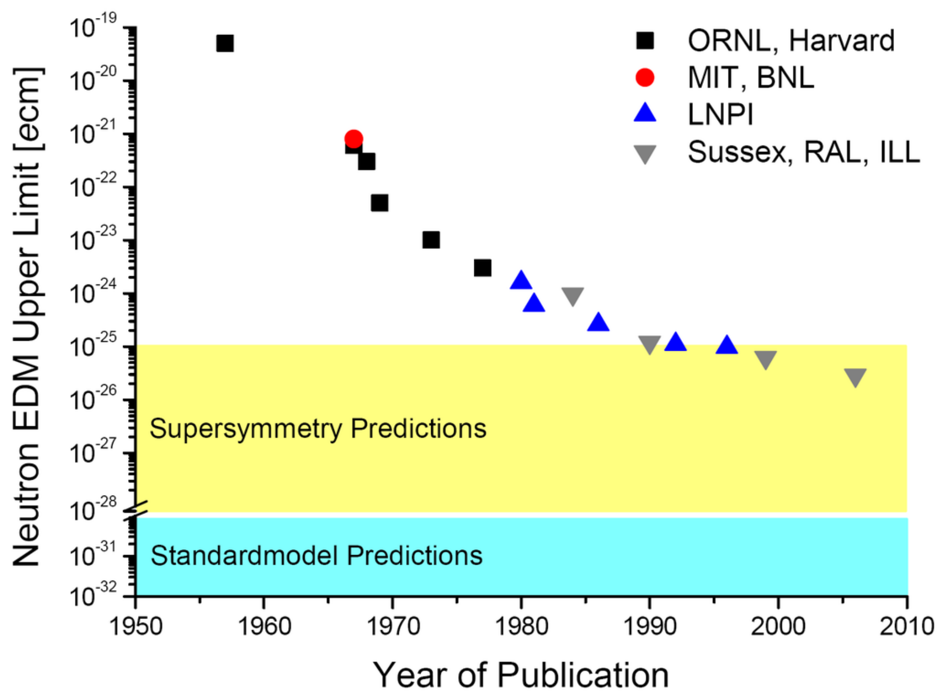

Figure 1.2: Historical limits of the nEDM: The ranges predicted for SUSY and Standard Model are highlighted in yellow and blue respectively. The black squares are measurements done at the Oak Ridge National Laboratory (ORNL). The red circles are experiments done at the Massachusetts Institute of Technology (MIT). The blue triangles are experiments done at Petersburg Nuclear Physics Institute (PNPI/LNPI). The grey triangles are experiments done as a collaboration among Sussex University, Rutherford Appleton Laboratory (RAL), Institut Laue–Langevin (ILL) [14]. Measured upper limits are at the 90% confidence level.

on the order of $\frac{n_{\mathrm{B}}}{n_{\gamma}} \approx 10^{-18}$ according to the Standard Model of particle physics[1]. This clear difference can be rectified by extensions to the Standard Model such as SUSY. Thus, a verification of models beyond the Standard Model have many exciting implications for modern physics.

The graph in Fig. 1.2 shows the evolution of limits on the nEDM over time. Over the course of 60 years the measurement precision of the upper limit on the nEDM has been improved by 6 orders of magnitude. The current best measurement has been set at $d_{\mathrm{n}} = (0.0 \pm 1.1_{\mathrm{stat}} \pm 0.2_{\mathrm{sys}}) \times 10^{-26}$ $e$cm by [7]. This corresponds to an upper limit of $|d_{\mathrm{n}}| < 1.8 \times 10^{-26}$ $e$cm with a 90 % confidence level.

The TUCAN collaboration aims to improve this limit by using a next generation UCN source by one order of magnitude, delving further into the regime of SUSY's predictions for the value of the nEDM, potentially ruling out such extended theories [17].

1.3 Ultracold Neutrons

A UCN is a slow-moving neutron with a kinetic energy less than 300 neV. This section will describe behaviors of UCN which make them ideal for performing an nEDM measurement, beginning with their interaction with surfaces, the methods by which they can be produced, and the loss channels. For the UCN source at TRIUMF, neutrons are produced using the proton beam from the cyclotron and directing it onto a tungsten target. This proton irradiation produces spallation neutrons which then must be cooled to UCN levels. The process by which this happens will be detailed below.

As E. Fermi first showed these UCN interact with materials as if they were constant potentials as opposed to individual nuclei [18]. The de Broglie wavelength of the UCN is of the order of 100 nm, therefore the UCN interact with the average of the potential of the strong interaction with several nuclei [18] [19]. Depending on the neutron scattering length of the material, this may result in an effective barrier. This potential is the Fermi potential (V_{F}), which is the sum of its real (V) and imaginary (W) components [20]. These components are defined in Eqn. 1.6. Thus, UCN can be confined within bottles and guides with sufficiently high potentials. Within these guides the UCN behavior can be compared to that of a thin cool gas, which diffuses within available volume. The real and imaginary potentials of a surface can be described by the equation [19]

$$V = \frac{2\pi h^2}{m} Nb, \, W = \frac{\hbar}{2} N\sigma v. \tag{1.6}$$

Within this equation m and v refer to the mass and velocity of the neutron, respectively. N is the atom's number density. b is the bound coherent scattering length. σ is the loss cross-section [21].

The Planck constant is h, and the reduced Planck constant is $\hbar$.

In this energy regime gravitational potential energy becomes a significant factor in the UCN's movement. Depending on the kinetic energy of the UCN, it is limited to a certain accessible height. These effects will be discussed in more detail in Chapter 4. The gravitational potential energy is defined as:

$$E_{\mathrm{grav}} = m_{\mathrm{n}} g h = 1.0252\,\mathrm{neV/cm} \times h. \tag{1.7}$$

Where h is the height in cm, m_{n} is the neutron mass, and g is the gravitational constant. UCN with energy E and incident angle θ reflect totally from a surface with a Fermi potential V_{F} under the conditions defined in Eqn. 1.8, where θ_c is the critical angle and V_{F} is the Fermi potential, which is fully defined in Eqn. 1.6. This interaction is defined as:

$$E \sin^2\theta \leq V_{\mathrm{F}} \sin\theta \leq \sin\theta_c \sin\theta_c = \left(\frac{V_{\mathrm{F}}}{E}\right)^{1/2}. \tag{1.8}$$

The use of an appropriate material allows UCN to be stored and transported between locations. However, the UCN must first be produced. Earlier experiments utilized a turbine to slow neutrons to the appropriate energy range [22]. However, the density of UCN produced by this method is too small for contemporary competitive nEDM searches. In work done by Korobkina and Golub it was shown that the production of UCN in superfluid Helium-4 was higher than thermal equilibrium would allow [23]. Ultimately this was shown to be due to the downscattering of incident thermal neutrons on resonant phonons. This realization spawned a generation of superthermal UCN sources [24]. The steady state density of UCN in a volume (ρ_{UCN}) is given by Eqn. 1.9, where P is the production rate and τ is the storage lifetime of the volume in which the UCN are produced [23]. This storage lifetime is inversely related to the loss parameters as discussed in Section 1.3.2. The production rate is then defined as:

$$\rho_{\mathrm{UCN}} = P\tau. \tag{1.9}$$

Superfluid He was chosen as the production material in order to fulfill specific theoretical criteria for a good UCN production source [25]. These conditions were defined by Golub and Pendlebury in 1977 as the following [26]:

1. A vessel filled with a medium with very small or no UCN absorption.
2. This medium has a critical energy for total reflection much less than the material which the walls are composed of.
3. The medium interacts with UCN as if there was only a single excited state with energy (E) $T(E) \ll T \ll T(E_\mathrm{u})$ with T being the temperature of the medium and E_u being the UCN's energy.

^{4}He is one of the few materials which can satisfy all of the above conditions, and several experiments have demonstrated its capacity for generating a high UCN density [27]. Helium-4 is preferred over Helium-3 as the latter has a very high neutron absorption cross section.

The improvement in UCN production density was significant, from $\rho_\mathrm{UCN} \leq 1\ \mathrm{n/cm}^3$ to $\rho_\mathrm{UCN} 1 \times 10^3\ \mathrm{n/cm}^3$ [26]. Superfluid He also has good properties for the storage of UCN, which also contributes to the higher production density. The historical improvement in UCN density can be seen in Fig. 1.3, with a sharp increase as superfluid sources came into use and a plateau approaching the theoretical density.

The contributions to the UCN production in helium can be split into the single phonon and multiphonon scattering channels [23]. The single phonon downscattering occurs at the resonant wavelength of 8.9 Å where the cross section for the interaction is highest. This corresponds to an energy of approximately 1 meV. The multiphonon excitation occurs along the tail of the dispersion relation. The contributions of these channels can be determined by the differential cross section for neutron scattering and are described in detail below.

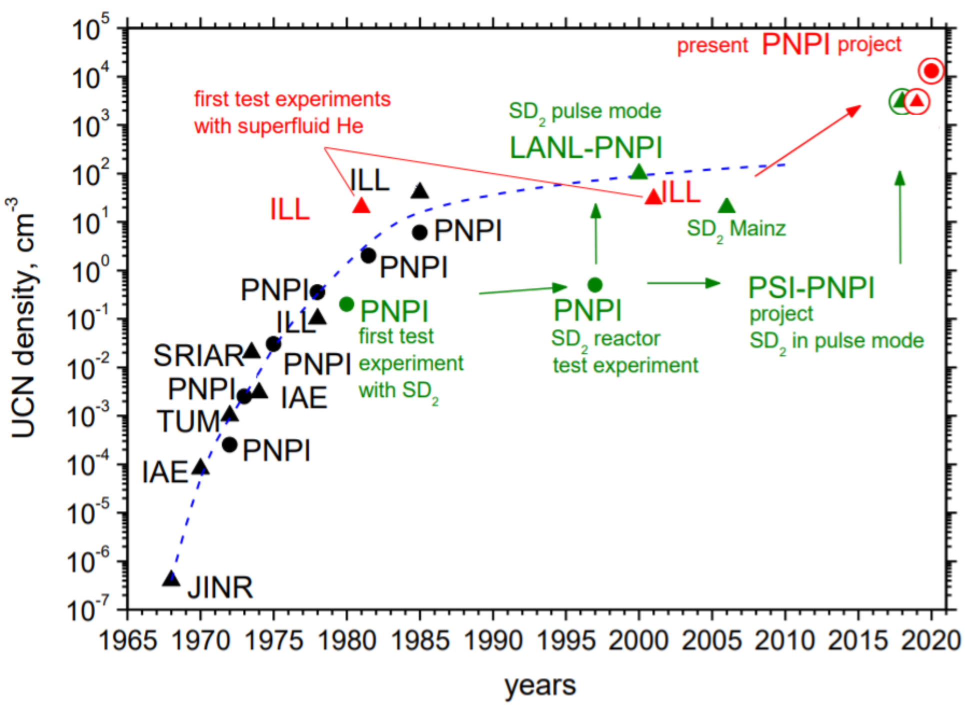

Figure 1.3: Evolution of UCN production density in different sources as reported by PNPI in their development of their UCN source. The dashed blue line illustrates the projected plateauing of the UCN density in the superfluid He sources. Green and red points are illustrating the development of the UCN source at PNPI to its most recent reported density, where the black points are historical densities. In green are tests done using solid deuterium (SD). Finally, in red are the runs done using the superfluid Helium. The steady state density reported by PNPI in 2020 was above 10^4 n/cm^{-3}, which is more than the predicted steady state density 10^3 n/cm^{-3}. The more recent UCN sources ILL and PNPI can be seen on the right. The other UCN sources are Scientific Research Institute of Atomic Reactors (SRIAR), Kurchatov Institute of Atomic Energy (IAE), Technical University Munich (TUM), and Joint Institute for Nuclear Research (JINR) [28].

1.3.1 Phonon Downscattering

Neutron downscattering in helium is the process by which one can produce UCN. To understand this behavior one may consider an incident neutron with mass m, momentum given by $\hbar q$ (with q being the wave vector), and energy given by $\hbar\omega$ (with ω being the frequency of the neutron) such that:

$$\omega = \frac{\hbar q^2}{2m} = \frac{\alpha q^2}{2}, \tag{1.10}$$

with $\alpha \equiv 41.14$ meV Å[23].

A neutron travelling with this energy and momentum can be brought to rest by transferring its energy and momentum into the superfluid ^{4}He via inelastic scattering [23]. Through the single phonon channel the magnitude of this energy and momentum transfer is determined by the dispersion relation:

$$\omega = \omega(q) = cq, \tag{1.11}$$

with c being the speed of light. Using a linear correspondence between the dispersion relation and the momentum transfer in Eqn. 1.11 is an approximation used to make the derivation more concise. For the case of cold neutron scattering this approximation is good. Therefore the incident neutron can come to rest, i.e. enter the UCN energy realm, by the emission of a single phonon only if they are at the resonant energy found by setting Eqn. 1.10 and Eqn. 1.11 equal. By doing this one can solve for the resonant energy (q^*) as follows:

$$cq^* = \frac{\hbar q^* 2}{2m} \rightarrow q^* = \frac{2mc}{\hbar}. \tag{1.12}$$

As previously mentioned, the resonant energy defined in Eqn.1.12 corresponds to neutrons with a wavelength of 8.9 Å [23]. In order to downscatter by a single phonon process, the incident neutron needs to be at this wavelength. In this energy range the neutron is referred to as a cold neutron.

UCN production is more efficient if incoming neutrons have previously been moderated to cold energies.

Neutrons may also downscatter via a multi-phonon process, which also contributes to the total production of UCN. In order to determine the scale of this contribution the differential cross section for neutron scattering $\left(\frac{d\sigma}{d\omega}\right)$ must be determined [26]. This cross section is determined by taking the Fourier transform of the van Hove correlation function ($S(q,\omega)$) which has been measured very precisely in several papers by Gibbs [29]. The cross section is related to the van Hove correlation function as:

$$\frac{d\sigma}{d\omega} = b^2 \frac{k_2}{k_1} S\left(q,\omega\right) d\Omega. \tag{1.13}$$

Where b is the scattering length, k_2 is the final wave vector, and k_1 is the initial wave vector. The relation $d\Omega = 2\pi \frac{qdq}{k_1 k_2}$ [23] can be substituted into Eqn. 1.13 which gives the result:

$$\frac{d\sigma}{d\omega} = \pi b^2 S(q,\omega) \frac{qdq}{k_1^2}. \tag{1.14}$$

Limits can be put on the range of q over which $S(q,\omega)$ needs to be considered. These limits are as follows:

$$k_1 - k_2 < q < k_1 + k_2 \text{ and } k_2 = k_{\mathrm{u}} \ll k_1 \text{ and } q \approx k_1, \tag{1.15}$$

where $\hbar k_{\mathrm{u}}$ is the momentum of the UCN. By Eqn. 1.15 one can see that the largest possible change in momentum is $dq = 2k_{\mathrm{u}}$. Using this and the assumption that $S(q,\omega)$ is constant over the small range dq one can state that

$$\frac{d\sigma}{d\omega} = 4\pi b^{\frac{k_{\mathrm{u}}}{k_1}} S\left(k_1, \omega = \frac{\alpha k_1^2}{2}\right). \tag{1.16}$$

One can then use Eqn. 1.16 in the definition for UCN production rate as follows:

$$P(E_{\mathrm{u}})dE_{\mathrm{u}} = \left[\int \frac{d\Phi(E_1)}{dE} N_{\mathrm{He}} \frac{d\sigma}{d\omega}(E_1 \to E_{\mathrm{u}}) dE_1\right] dE_{\mathrm{u}}, \tag{1.17}$$

which becomes

$$\int_0^{E_\mathrm{c}} P\left(E_\mathrm{u}\right) dE_\mathrm{u} = N_\mathrm{He} 4\pi b^2 \alpha^2 \left[\int \frac{d\Phi(k_1)}{dE} S\left(k_1, \omega = \frac{\alpha k_1^2}{2}\right) dk_1 \right] \int_0^{k_\mathrm{c}} k_\mathrm{u}^2 dk_\mathrm{u} \tag{1.18}$$

$$= N_\mathrm{He} 4\pi b^2 \alpha^2 \left[\int \frac{d\Phi(k_1)}{dE} S\left(k_1, \omega = \frac{\alpha k_1^2}{2}\right) dk_1 \right] \frac{k_c^3}{3} \ \mathrm{UCN\ cm^{-3} s^{-1}}. \tag{1.19}$$

The values E_c, k_c are the critical UCN energy and wave vector of the vessel's walls respectively, corresponding to the energy at which UCN can be produced. The energy spectrum of the incident neutrons is represented by $\frac{\Phi(k_1)}{dE}$. The number density of the medium is N_He. In order to find the contributions of the single phonon or multiphonon contributions one simply integrates over the appropriate energy range. For the single phonon contribution one integrates over the single phonon peak. This peak is approximated as a delta function centered at the intersection of the ^{4}He and neutron dispersion curves. This intersection occurs at 0.706 Å^{-1} [23].

Multi phonon contributions are due to the broadening of the dispersion relation as can be seen in Fig. 1.4. Where the single phonon downscattering occurs at the intersection of the black line and the neutron dispersion curve, the multi phonon downscattering occurs via multiple down scatters in the gray region above this curve [23]. The UCN density saturates at the point where the loss modes of UCN equals the production rate. These loss modes are explored in the following section.

1.3.2 UltraCold Neutron Losses

In the definition of the steady state in Eqn. 1.9 the total UCN density is a function of both the production and the UCN loss modes, represented by the storage time τ. This storage lifetime is inversely related to the loss probability. The production rate is mostly stable in the range of temperature fluctuations expected in the cryostat, but the loss modes are strongly temperature

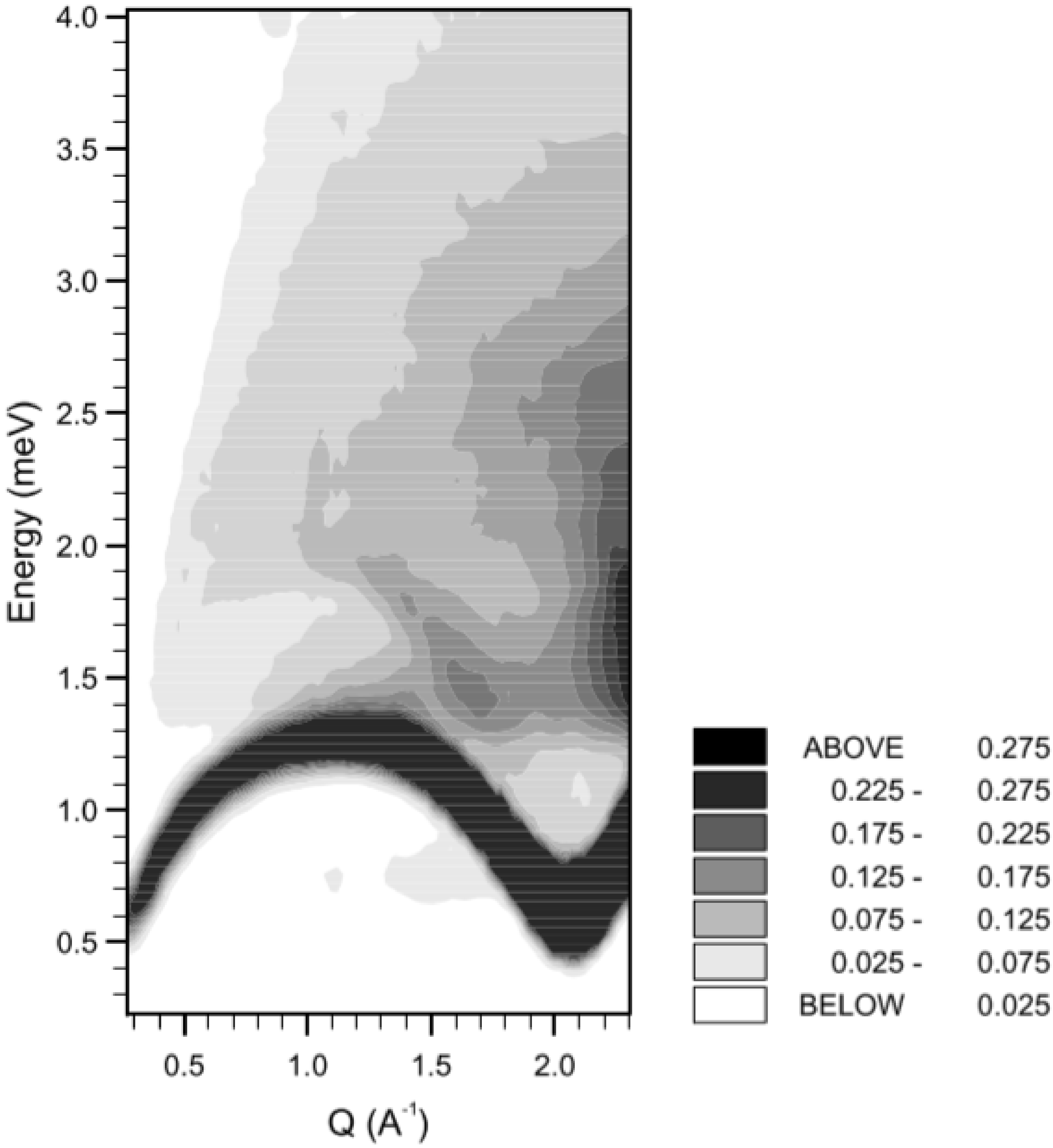

Figure 1.4: A contour plot of the relation between the single excitation energy and incident wave vector for superfluid ^{4}He. The range of shades are proportional to the scattering intensity in meV^{-1}. The black region is the area in which single phonon downscattering may occur, whereas the grey regions are regions in which multiphonon downscattering may occur. The intersection of these regions and the neutron dispersion relation gives the wavelengths at which the most UCN downscattering occurs [30].

dependent. Therefore one of the best methods for improving the UCN density is reducing the UCN loss modes. UCN are lost through the following processes [31]:

1. up-scattering by phonons in the superfluid ^{4}He,
2. inelastic scattering by He gas molecules,
3. absorption by ^{3}He,
4. wall losses,
5. leakage through holes,
6. neutron β-decay.

This loss probability is quantified by a summation of the individual contributions τ_i to the final τ

$$\frac{1}{\tau} = \sum_i \frac{1}{\tau_i}. \tag{1.20}$$

For the purposes of this thesis the most important loss processes are wall losses and leakage through holes or slits.

Wall Loss

The majority of UCN interact with surfaces by reflecting off them, given a sufficiently high surface potential. However, some of them will interact inelastically via scattering or absorption by a nucleus. The corresponding lifetime for this wall loss process is labelled τ_{wall}. The vessel surface appears to the UCN as a complex step in the Fermi potential.

In Eqn. 1.6 the potential seen by the UCN interacting with a material has been defined. From this one can define a wall loss probability per bounce (μ) as a function of energy (E) and incident angle (θ) from the surface normal

$$\mu(E,\theta) = 2\eta\left(\frac{E\cos^2\theta}{V - E\cos^2\theta}\right)^{1/2}. \tag{1.21}$$

The factor η is a wall loss parameter defined by

$$\eta = \frac{W}{V} = \frac{\sigma_l k_i}{4\pi b}. \tag{1.22}$$

Where σ_l is the sum of the inelastic and absorption cross section. k_i is the incident wavevector.

UCN in a closed vessel can be treated as a cold thin isotropic gas after several wall collisions. Therefore, it is more useful to consider the average of μ over angles of incidence for a specific E:

$$\bar{\mu}(E) = 2\eta\left[\frac{V}{E}\sin^{-1}\left(\frac{E}{V}\right)^{1/2} - \left(\frac{V}{E} - 1\right)^{1/2}\right]. \tag{1.23}$$

Depending on the quality of the vessel in which the UCN are produced, diffuse reflection can become a factor in the wall interactions. Some of the UCN will be reflected diffusely, following the cosine law, where $P(\theta)$ is reflection probability of a particle leaving the surface at angle θ into solid angle $d\Omega$:

$$P(\theta)d\Omega = \cos\theta d\Omega. \tag{1.24}$$

The total reflection is a mixture of the diffuse and specular reflection, with corresponding probabilities f and $1-f$ respectively. For a good surface, with high quality polish the diffuse reflection follows $f \to 1$. Ultimately the contribution to the storage lifetime of the wall loss takes the form:

$$\frac{1}{\tau_{\text{wall}}} = \frac{\bar{\mu}(E)vA_{\text{surf}}}{4V} = \bar{\mu}(E)\frac{v}{l}. \tag{1.25}$$

Where v is the velocity of the UCN within the vessel, V is the volume of the vessel, and A_{surf} is the surface area of the vessel. In the final part of the definition $l = \frac{4V}{S}$ is introduced as the mean free path of the UCN in the vessel.

Hole Leakage

The contribution of leakage from holes or gaps in the UCN guides is simply represented as a wall loss with $\mu = 1$ such that

$$\frac{1}{\tau_{\mathrm{leakage}}} = \frac{vA_{\mathrm{hole}}}{4V}, \tag{1.26}$$

where A_{hole} is the area of the hole or gap.

1.3.3 UltraCold Neutron Energy Spectrum

The initial energy spectrum of the UCN produced via ^{4}He downscattering during the proton irradiation is assumed to follow a square root distribution, as the tail of the Maxwell distribution. This is described by:

$$N_{\mathrm{UCN}}(E) \propto \sqrt{E}. \tag{1.27}$$

Where N_{UCN} is the number of UCN at any given energy (E). Within the regime of UCN kinetic energy the effect of the gravitational potential energy is significant to their movement in the guides, and their interactions at surfaces. Part of the process of characterizing UCN experimental setups is understanding the initial spectrum of the UCN and how they interact with the materials within the setup.

Measurements of the produced UCN spectrum can be performed utilizing the gravitational interaction of the UCN, which are limited by the accessible height h which is proportional to the energy of the UCN $E_{\mathrm{UCN}} = m_{\mathrm{n}}gh = 1.0252\ \mathrm{neV/cm} \times h$. Some examples of these experimental methods are the spectrum bottle (described in Chapter 4) and the gravitational inverted U-bend. Both of these setups work by cutting out specific parts of the UCN energy spectrum by either providing a height barrier over which only the higher energy UCN can pass, or an absorber which cuts out only the neutrons with enough energy to reach the absorber set to a specific height, allowing only the low energy neutrons through.

1.4 PENTrack Simulations

The simulation framework PENTrack has been specifically developed for UCN. Throughout the runs of the TUCAN experiments PENTrack has been used to benchmark simulations against experiments that have been performed, and to plan for future experiments. The code currently resides in a repository on GitHub [32].

The physics that drives PENTrack can be categorized into the equation of motion, the interactions with matter, and the spin of the neutrons, so that their behavior in an EDM cell can be quantified. These mechanics are described in detail in Wolfgang Schreyer's paper on PENTrack [33].

Briefly, for particles traveling though space in PENTrack the following forces will be acting upon them, where vectors are represented in bold:

- Force of gravity $m\mathbf{g}$,
- Lorentz force $q(\mathbf{E} + \dot{\mathbf{x}} \times \mathbf{B})$,
- Force of magnetic gradient on magnetic moment $p\mu\nabla|\mathbf{B}|$.

Therefore, the total force will go as:

$$\mathbf{F} = m\mathbf{g} + q(\mathbf{E} + \dot{\mathbf{x}} \times \mathbf{B}) + p\mu\nabla|\mathbf{B}|. \tag{1.28}$$

Where Eqn. 1.28 refers to a particle of mass m, charge q, magnetic moment μ, gravitational constant g, magnetic field $\mathbf{B}$, electric field $\mathbf{E}$, and polarization of p.

Presently, interactions with matter are only defined for neutrons in PENTrack, and the modeling of these interactions is based primarily on the complex Fermi potential assigned to the material. This potential determines absorption, transmission, and reflection cross sections of the material when the neutron interacts with its surface. In order to simulate reflections there are two available models implemented in PENTrack: the Lambert reflection model [34] [35] and the Micro-Roughness model. The Lambert reflection model follows the definition in Eqn. 1.24, with the cosine dependent intensity. The Micro-Roughness model describes the diffuse reflection using a Gaussian correlation function [36] [37].

Finally, the precession of the spins and their interaction with the fields is modeled using the Bargmann-Michel-Telegdi equation (BMT) [38]. As the particle moves through space this equation is integrated separately from the equation of motion. Additional flipping of the spins may occur at surfaces, which is determined by a user assigning a spin flip probability per bounce to the materials in their geometry.

As discussed, the behavior of UCN at surfaces is determined in part by the Fermi potential of that surface, as well as the polish of the surface. Each of these parameters corresponds to a tunable input in the simulation configuration files, the Fermi potential and Micro-Roughness respectively. Different qualities and polishes of guides may cause variances in these behaviors from the theoretical predictions. Often the simulated material properties will be tuned from initial values to known experimental data in order to account for these differences. This is a process referred to as benchmarking.

Recent updates of the software have allowed for the definition of a loss-per-bounce probability akin to the spin flip probability. Some recent simulations have varied from experimental results by a significant amount. It is possible that in the energy range considered for UCN this energy dependent absorption model is incorrectly describing the UCN wall loss. This newly implemented change becomes relevant for results in Chapter 4 [39]. The update took place after the work done in this thesis, but the results in Chapter 4 indicate that the previous model generated results which disagreed with experimental findings.

CHAPTER 2

EXPERIMENTAL SETUP AT TRIUMF

This chapter contains a description of how the UCN source works at TRIUMF beginning at the acceleration of the negative hydrogen ions. From the acceleration of these ions in the cyclotron the proton beam is produced. Bunches of protons are delivered via a beamline to the UCN experimental area in TRIUMF's meson hall, where they collide with a spallation target, producing free neutrons. The staged cooling process of these spallation neutrons is explained, followed by the downscattering in isopure ^{4}He which produces the UCN. The proposal for the nEDM spectrometer to be used in future experiments will be introduced.

Additionally, setups from experiments performed in 2018 relevant to the analysis in Chapter 3 will be described. Specifications of the two types of UCN detectors used in these runs will be given, as well as a brief description of the physics behind the neutron detection process.

2.1 Proton Beamline at TRIUMF for the Production of Spallation Neutrons

TRIUMF is the home of one of the world's largest cyclotrons, with the capacity to accelerate negative hydrogen ions to 75% of the speed of light. It produced its first beam in December of 1974 and continues its operation to this day. Beginning in a tank, negative hydrogen ions are accelerated in stages. The first stage is a series of resonators which oscillate at 23 MHz [40]. After this the particle bunch is injected into the center of the cyclotron where it enters and exits the dee structures synchronized with the RF cycle. With each crossing of the gaps between the dees, the particle bunch gains energy. This causes it to spiral outward and over the course of 326 μs it reaches its top speed [40]. After this acceleration phase, the hydrogen ions must be stripped of their electrons, resulting in a bare proton. This extraction is done using small graphite foils of 11 μm thickness [40]. Upon passing through this foil the electrons are stripped and only the positive protons remain. In the cyclotron's magnetic field they curve the opposite direction of the negative ions, causing them to exit the cyclotron where they are extracted into a proton beamline. The cyclotron at TRIUMF can produce up to four proton beams simultaneously at a range of energies from 70 to 520 MeV.

The TRIUMF beamline which provides the protons to the UCN spallation target was commissioned in 2016. An overview of the UCN facility, including the proton beamline, the UCN source, and the nEDM spectrometer is shown in Fig. 2.1. The beamline which delivers protons to the UCN experiment is referred to as BL1U. This proton beamline shares protons with another beamline referred to as BL1A, which provides protons for the Center for Material and Molecular Science instruments (CMMS) [41]. They are split by a fast-kicking magnet which ramps on and off during the 100 μs gap between consecutive proton pulses from the cyclotron [41]. This allows for the simultaneous beam delivery to both BL1A and BL1U.

In Fig. 2.2 a top down view of the new beamline with the components labelled can be found. This includes several monitors for beam position and current, as well as tuning magnets. An itemized list of these components can be found in Tab. 2.1. For the work done in this thesis, output from the beam intensity monitor 1UTNIM2 (which from here on will be abbreviated to TNIM2) and the behavior of the kicker magnet are being investigated.

The kicker magnet 1VK6 is used to split the proton beam from the cyclotron between BL1U and BL1A. The macrostructure of the beam is shown in Fig. 2.3. Some fraction of the beam is sent to the UCN target, up to a third of the pulses. In order to achieve this, the kicker magnet must ramp up in the 50 μs notch between these pulses, and ramp down in the same time frame. If the kicker magnet is ramping up or down outside of the pulse gaps it can cause beam spillage downstream in

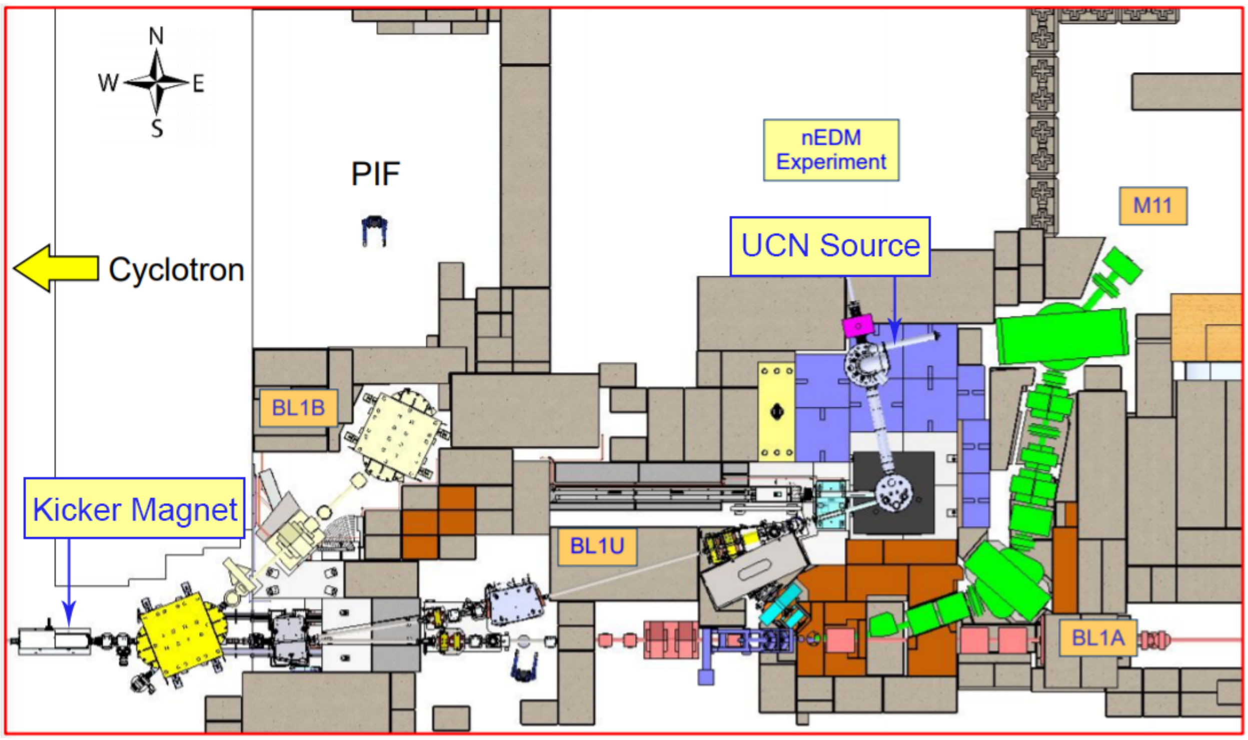

Figure 2.1: A rendering of the location of the new BL1U proton beamline in relation to BL1A and BL1B. The protons enter BL1A from the left. Radiation shielding blocks are represented in tan. The kicking magnet which splits BL1U from BL1B is shown in white. The proton beam is brought to the spallation target in the dark grey section, where the UCN production happens. Then the UCN are guided to the area labelled nEDM Experiment [42].

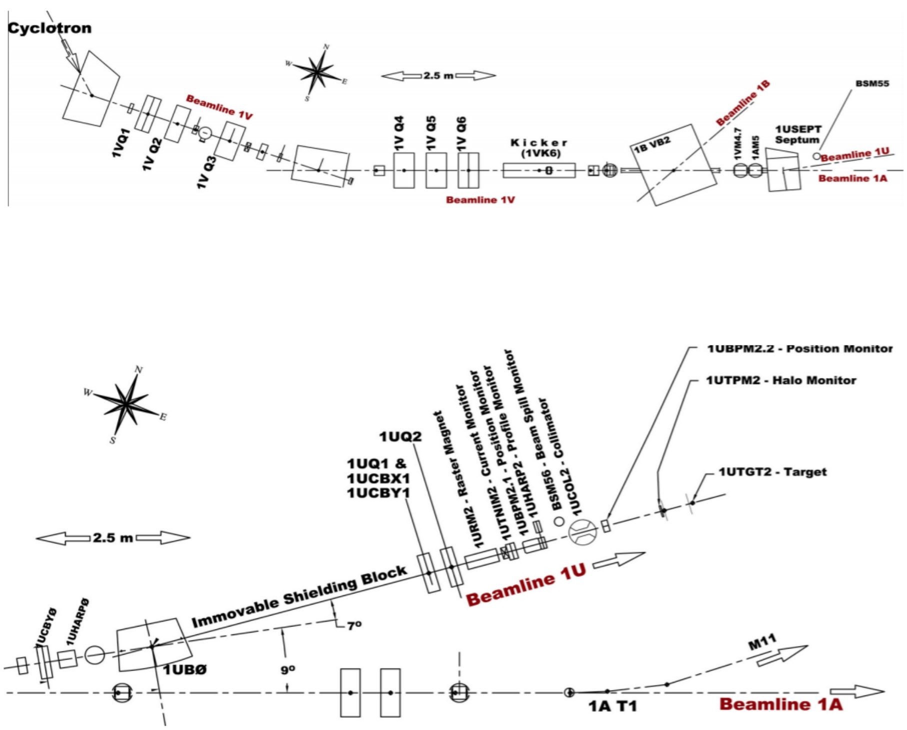

Figure 2.2: (top) Top view of beamline structure from the Cyclotron to the UCN source, showing the branching of BL1B, BL1A, and BL1U from the main BL1V, and details of the focusing magnets along the beamline. (bottom) Top view detail of the branch between BL1A and BL1U, with labelled elements which are given in Tab. 2.1. The labelled components are responsible for the monitoring and the tuning of the beamline [41].

Beamline Element	Type
1AM4.7	beam position monitor
1AM5	HARP wire chamber
1BVB2	dipole bender
1UB0	bending dipole
1UBPM2.1, 1UBPM2.2	beam position monitors
1USEPT	septum magnet
1UCBY0	vertical correction steerer
1UCBX1, 1UCBY1	horizontal and vertical steerers
1UCOL2	collimator
1UHARP0, 1UHARP2	HARP wire chamber
1UQ1-Q2	quadrupole doublet
1URM2	raster magnet (Planned)
1UTNIM2	current monitor
1UTNPM2	beam halo monitor
1VQ1-Q6	two quadrupole triplets
1VK6	kicker magnet
1VM4	notch monitor
BSM55, BSM56	beam spill monitor

Table 2.1: Table of devices along the beamline as detailed in Fig. 2.2.

the septum magnet 1USEPT.

BL1U delivers 483 MeV of proton beam up to a current of 40 μA to the UCN target, which is made of tungsten. Protons colliding with this target generate spallation neutrons. This target is surrounded by lead blocks and placed below the UCN source. The target is irradiated by 1/3 of the proton beam for a period of time called the production period, usually about 60 s.

2.2 The Vertical UCN Source Cryostat

The UCN cryostat currently installed at TRIUMF has been developed and tested at the Research Center for Nuclear Physics for the University of Osaka (RCNP). The cryostat contains the UCN production volume which is a cylindrical bottle holding 8 L of superfluid isopure Helium-4 ori-

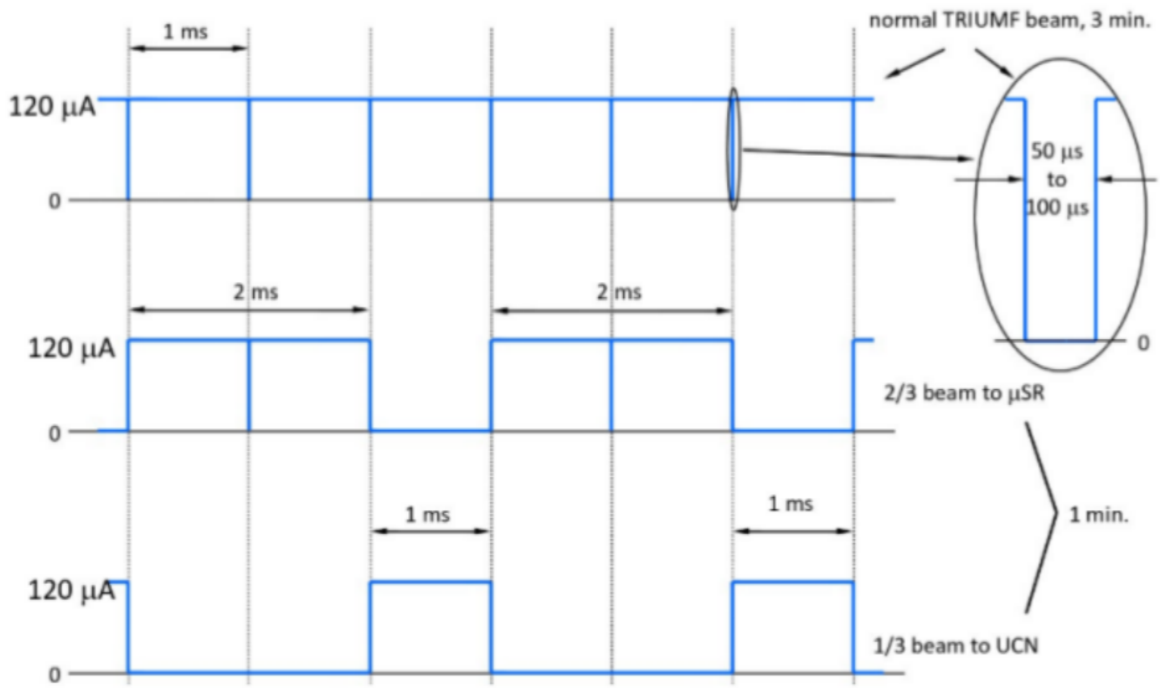

Figure 2.3: Pulse structure of BL1V where 1/3 of the beam is delivered to BL1U and 2/3 are delivered to BL1A. The topmost structure is the normal proton beam from the cyclotron at 120 μA over approximately 7 ms. This is composed of 1 ms pulses with 50-100 μs gaps. The second structure is the beam delivered to BL1A and the third is the beam delivered to BL1U [43]. μSR refers to the instruments used in BL1A.

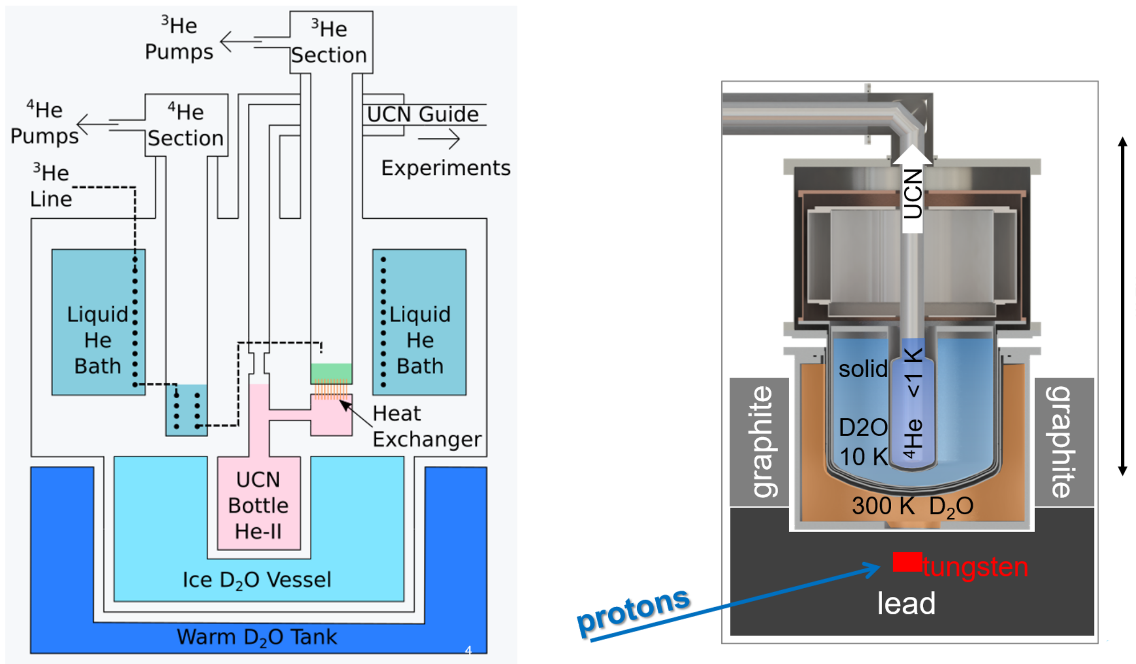

Figure 2.4: (left) Cross section of the moderators and UCN source. The connections of the staged ^{3}He cooling are indicated with dashed lines. The dotted lines are coils. The heat exchanger between the UCN bottle and the ^{3}He is shown with orange lines. (right) Cross section of UCN cryostat with the different moderators labelled. The temperature of each of the moderators is shown. Additionally, the position of the target relative to the cryostat is shown beneath the source cryostat, separated by layers of 300 K D_2O, and solid 10 K D_2O. The movement of the UCN upward and away from the production volume is indicated with the white arrow.

ented vertically. This volume is kept at a temperature below 1 K. This cryostat is a prototype which is being used while the future UCN source is in development. It was installed in 2017 after the finalization and commissioning of BL1U. Tests at RCNP have shown this source to have a cooling power which matches proton beam operation at only a few μA. The isotropically produced spallation neutrons pass through a series of moderators before reaching the UCN source itself.

The moderators and cryostat are shown in Fig. 2.4. The figure shows the layers of moderators through which fast spallation neutrons move before they reach the inner cryostat. The lead shields the cryostat from gamma rays, and the graphite reflects neutrons back into the cryostat. The liquid heavy water (D_2O) is at room temperature and the solid heavy water at 10 K. Both serve to moderate the neutrons to the cold energy regime (< 0.025 eV) as they move towards the source.

This is crucial as the cross section for UCN production in superfluid helium is maximal at cold neutron energies, as discussed in Section 1.3. The cold neutrons are then converted to UCN in the 1 K ^{4}He superfluid. The helium in the UCN production volume needs to be isotopically pure ^{4}He in order to avoid UCN losses due to the large neutron absorption cross section of ^{3}He.

Thus, there are three different fluid cycles within the UCN source cryostat which allows us to keep the isotropically pure ^{4}He at 1 K levels. These cycles are the isotopically pure ^{4}He for UCN production, natural abundance ^{4}He for precooling, and ^{3}He for the final cooling stage. Cooling is done with ^{3}He in order to achieve lower temperatures due to its advantageous vapor pressure. The isopure ^{4}He is cooled in various stages. First in the liquid helium bath supplied from the TRIUMF liquifier facility which cools the isopure ^{4}He to 4.2 K. Then pumping on the ^{4}He volume cools it to 1.6 K. Finally pumping on the ^{3}He volume, which is connected to the isopure volume via a heat exchanger, brings it below 1 K.

Through these stages the UCN source achieved a cooling power of approximately 300 mW at 0.9 K. This cooling power can only remove a heat load corresponding to approximately 1 μA of primary proton beam while keeping the temperature constant. However, that is insufficient beam intensity to produce the desired UCN density in the source. Higher proton beam intensity produces more spallation neutrons, but also increases the heat load, therefore requiring more cryogenic cooling power. This is the motivation for the ongoing design and commissioning of a new UCN source at TRIUMF, based on what has been learned from the installed prototype source. The future source is designed to have a cooling power of 10 W at a temperature of 1.1 K [41].

2.3 TUCAN's nEDM Spectrometer

The nEDM spectrometer which will be used in the TUCAN next generation nEDM experiment is still in development. This nEDM spectrometer is designed to utilize Ramsey's method of separated oscillating fields [44]. The general approach for using Ramsey's method to measure the nEDM is described below, as well as the developmental status of TUCAN's nEDM spectrometer.

The Ramsey method measures the Larmor precession frequency of a spin polarized particle in a magnetic field. If the particle has an electric dipole moment the presence of an electric field will modify this frequency. In order to extract a value for the electric dipole moment the precession frequencies for a neutron with a magnetic dipole moment (μ_{n}) and electric dipole moment ($\mathbf{d}_{\mathrm{n}}$) in parallel and anti-parallel magnetic and electric fields are compared. Given a magnetic field $\mathbf{B}$ and a collinear constant electric field $\mathbf{E}$ the precession frequency of the neutron(f_{n}) is given by:

$$hf_{\mathrm{n}} = |2\mu_{\mathrm{n}}\mathbf{B} \pm 2\mathbf{d}_{\mathrm{n}}\mathbf{E}|, \tag{2.1}$$

where h is the Planck constant. The $\pm$ corresponds to parallel and anti-parallel electric and magnetic fields, respectively. Therefore by measuring both the precession frequency of the parallel and anti-parallel setups an expression for the nEDM (d_{n}) can be extracted:

$$f_{\mathrm{n}}^{\uparrow\uparrow} - f_{\mathrm{n}}^{\uparrow\downarrow} = \frac{1}{h}\left(2\mu_{\mathrm{n}}B^{\uparrow\uparrow} - 2\mu_{\mathrm{n}}B^{\uparrow\downarrow} + 2d_{\mathrm{n}}E^{\uparrow\uparrow} + 2d_{\mathrm{n}}E^{\uparrow\downarrow}\right), \tag{2.2}$$

$$d_{\mathrm{n}} = \frac{h(f_{\mathrm{n}}^{\uparrow\uparrow} - f_{\mathrm{n}}^{\uparrow\downarrow}) - \mu_{\mathrm{n}}(B^{\uparrow\uparrow} - B^{\uparrow\downarrow})}{2(E^{\uparrow\uparrow} + E^{\uparrow\downarrow})}. \tag{2.3}$$

Thus, the small value of the nEDM can be extracted via a high precision measurement of the difference in precession frequencies between the parallel and anti-parallel field configurations. However, care must be taken in the measurement to avoid a false signal [45]. Ideally the magnetic field $B^{\uparrow\downarrow}$ and $B^{\uparrow\uparrow}$ would be the same, which would make the measurement independent of the

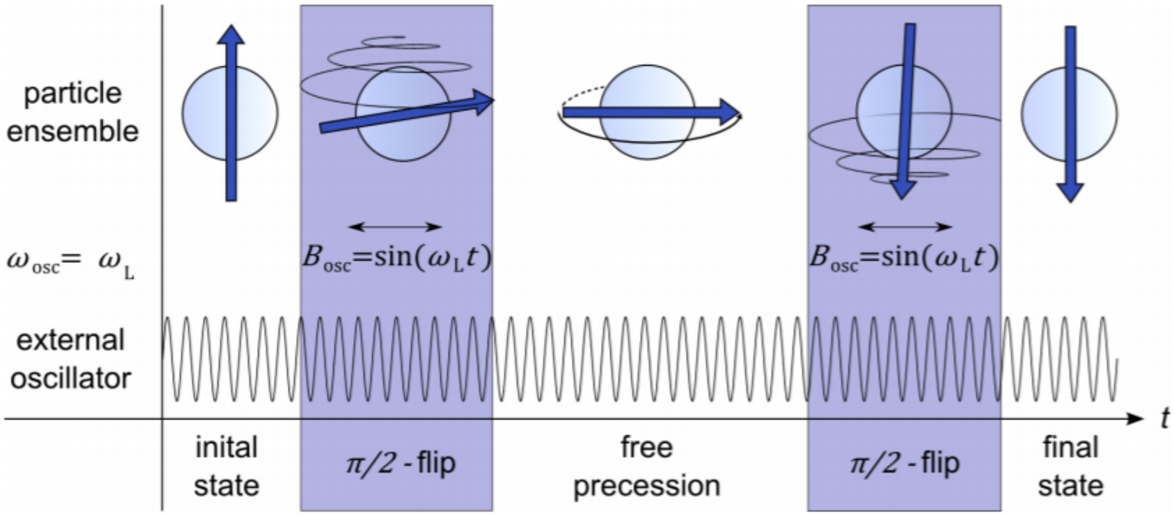

Figure 2.5: A visual depiction of the steps of the Ramsey method. The particle ensemble in its initial polarized state undergoes a $\pi/2$ flip after an oscillating magnetic field is applied at frequency ω_{L} for time τ. It is then allowed to precess freely for a set time (T), after which a second pulse is applied, for the same amount of time flipping it by another π/2 [46].

magnetic field as the two terms in Eqn. 2.2 will cancel out. Failing that, a precise measurement of the difference in the magnetic field between the two configurations is crucial to the precision of the final nEDM measurement. Additionally Eqn. 2.2 shows that a high electric field will increase the difference between the measured frequencies, increasing the sensitivity of the measurement. Both factors are major considerations in the design of TUCAN's future nEDM spectrometer.

The steps of the measurement method can be seen in Fig. 2.5. The phases of this measurement are described below.

1. In the initial phase the neutron ensemble is in the constant magnetic holding field (B_0), with magnetic moment aligned.

2. During the second phase the first pulse of the oscillating magnetic field B_{osc} is applied with a frequency of ω_{L}. During the first pulse the spins of the polarized neutrons are tipped into the plane perpendicular to B_0.

3. During the third phase the spins of the neutrons are freely precessing around B_0.

4. In the final phase another pulse of the oscillating magnetic field B_{osc} is applied with a frequency of ω_{L}. If the frequency of B_{osc} is equal to the Larmor precession frequency then the spins of the neutrons will tip $\pi/2$, flipping the polarization to the opposite of its original orientation.

If the frequency of the oscillating magnetic field is not equal to the resonance frequency ω_{L} then the neutrons will tip by a total amount less than π. The neutron spins are measured by filtering either the spin up or spin down neutrons and then counting how many remain in a UCN detector. In the measurement of the neutron spins the ratio of the spin up neutrons to the spin down neutrons will shift as the frequency of the oscillating magnetic field is shifted. A scan of B_{osc} reveals the resonance curves in this ratio [44].

In experiments which measure both spin up ($N_{\uparrow}$) and spin down ($N_{\downarrow}$) neutrons after the Ramsey cycle it is useful to define the asymmetry factor (A):

$$A = \frac{N_{\uparrow} - N_{\downarrow}}{N_{\uparrow} + N_{\downarrow}}. \tag{2.4}$$

Thus plotting this factor against the frequency of B_{osc} gives a sinusoidal resonance curve. The form of the resonance curve is shown in Fig. 2.6, which has been fit with the function defined in Eqn. 2.5, where A_{off}, α, and Φ are free parameters. The value $\Delta\nu$ is the calculated resonance line width. The asymmetry factor can then be expressed as:

$$A = A_{\text{off}} \mp \alpha \cos\left(\frac{\pi \Delta f}{\Delta\nu} + \Phi\right). \tag{2.5}$$

The measurements are performed near the working points of this Ramsey fringe. The working points are defined where the slope of the function is the steepest, and therefore most precise to fit. These points are defined using the fringe width $\nu = (2(\mathrm{T} + 4\tau/\pi))^{-1}$ as $f_{\text{n}} \pm 0.25\nu \pm 0.05\nu$. In

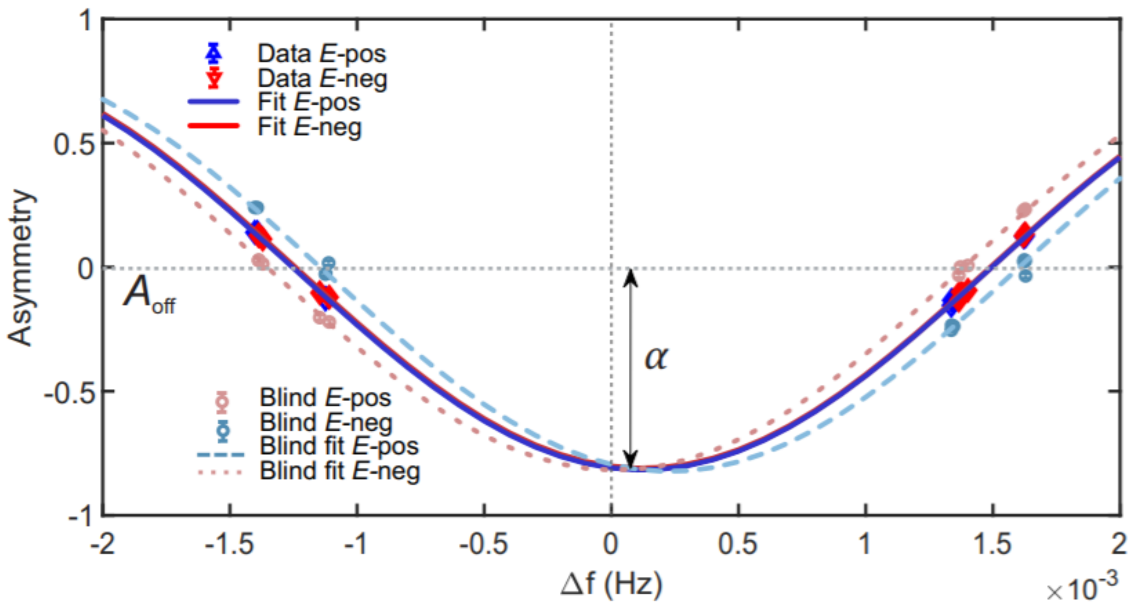

Figure 2.6: The measurement and fit of the central Ramsey fringe from the most recent measurement in search of the nEDM [7]. The asymmetry defined in Eqn. 2.4 is plotted against the frequency. Clusters of data can be seen in red and blue around the working points of the curve. The free parameter α defined in Eqn. 2.5 is labelled with a black arrow [7].

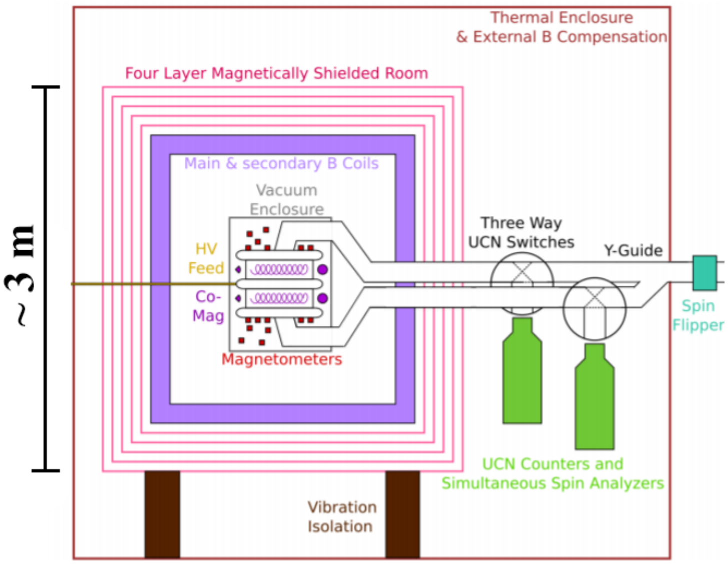

Figure 2.7: Simplified diagram of the nEDM spectrometer currently in development at TRIUMF. UCN from the source arrive from the right through the spin flipper, then directed via a 3 way switch, entering the two separate magnetically, thermally, and vibrationally shielded chambers in which the Ramsey cycles are performed with the fields aligned and unaligned simultaneously. The UCN are then guided to the UCN simultaneous counters and spin analyzers. The high voltage feed (HV feed) supplies current to the central electrodes. The magnetic fields are measured by the magnetometer and the comagnetometer [47].

Fig. 2.6 the data scatters can be seen around these four working points.

In order to achieve the desired sensitivity of 10^{-27} $e$cm at the TRIUMF UCN facility, the nEDM spectrometer has been designed to optimize the performance of this Ramsey cycle measurement on several fronts.

As can be seen in Fig. 2.7, the nEDM spectrometer will be placed in a magnetically shielded room to significantly reduce the background from fluctuations in the magnetic field over the course of the measurement. In addition, the co-magnetometers, which can measure the magnetic field within the EDM cells, will help correct for the magnetic field drifts and reduce the systematics of the setup. In the work of this thesis one of the primary analyses is done to improve the understanding of the detectors to ensure stability in the counts after the Ramsey cycle. Additionally, work is done to characterize the expected energy spectrum of the UCN from the source, which determines how many are UCN expected to survive the full Ramsey cycle run time [48].

2.4 The Experimental Setups for the UCN Beam Time in 2018

The scope of this thesis covers experiments performed during fall of 2018. Cryogenics and target of the UCN source were set up as previously described. In the 2018 run the intention was to test the relative storage and transmission efficiencies of guides with different coatings and surface qualities, as well as valves in different configurations which will be used in future experiments. These experiments are necessary to minimize the UCN losses during the transmission and measurement processes. The experimental configurations are referred to via the TCN18 designation for the 2018 run of the TUCAN experiment and then a secondary numeric designation. For each configuration, the runs were organized into supercycles, which are composed of several periods. Each of these periods has cycles of various lengths which designate periods with a specific valve state or component configurations. A single cycle corresponds to a single production period in the UCN source, normally over a period of 60 s, followed by a storage or transmission time.

The configuration within the radiation shielding is composed of the production volume and the cryogenic components. The UCN are produced up to the valve inside the shielding before the $45°$ kink. The kink is required in order to avoid a direct line of sight to the target. Simulations showed that a direct line of sight would cause too much radiation leakage into the meson hall, exceeding radiation limits for the hall. This configuration can be seen in Fig. 2.8.

A variety of configurations were measured, most falling into the category of measuring the transmission or storage of certain guides and components. Additionally, daily measurements were taken

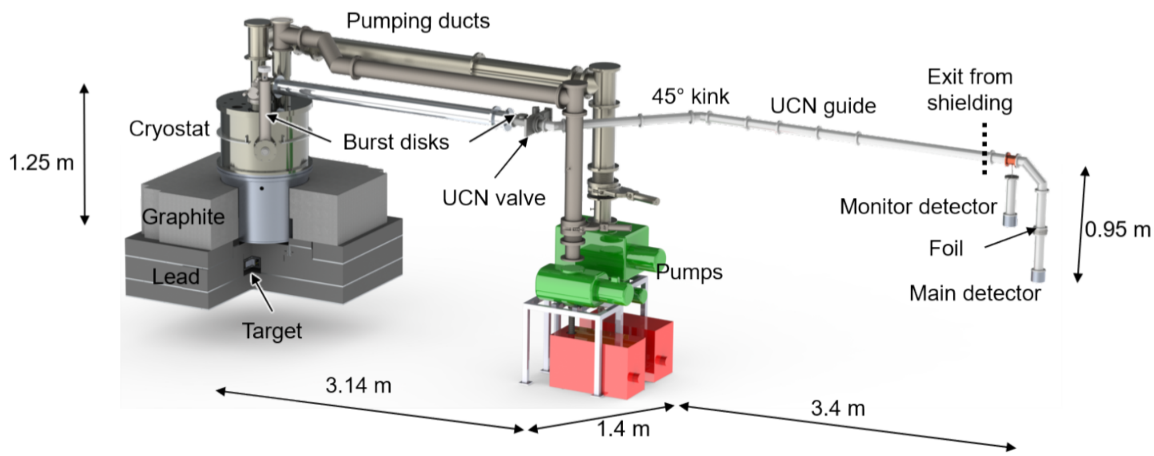

Figure 2.8: Rendering of the TRIUMF UCN source and guides past the radiation shielding. This setup is one of the most basic experimental set up used as a baseline for other transmission experiments. The distances are labelled in meters with black arrows. The graphite and lead moderators are shown around the target and cryostat, as well as the pumps which maintain the pressure within the experimental setup. The location where the guides exit from the radiation shielding is marked with a dotted black line [49].

of the storage lifetime within the source itself in order to monitor the evolution of the UCN source performance over the course of the beamtime. A brief discussion of these two types of measurements follows, to motivate the detector studies done in this thesis.

2.4.1 UCN Transmission and Storage Experiments

Transmission and storage measurements are two ways that one has of quantifying the behavior and performance of the guides and components used in UCN experiments.

Transmission experiments are a measurement of how many UCN travel through a component and can be counted in a detector, relative to how many UCN can be counted in a detector in the absence of that component. This component may be a guide, a valve, the nEDM spectrometer, etcetera. Results of a relative transmission measurement are determined by the ratio of the counts in a monitor detector to the counts in the main detector. In order to achieve significant statistics, measurements for each setup are repeated. This is a good quantification of how well guides with different surface materials and different polishing finishes may transmit UCN towards the final detector. Ultimately this will be a measure of how many UCN will be available in the main experiment: the future nEDM spectrometer, once it is developed.

A storage measurement is performed by isolating the UCN in the component under investigation by closing valves on either end of the component. In order to extract the lifetime of the UCN interacting with a material or component, one must store the UCN for various time intervals, normally between 0 and 500 s. In storage measurements such as this, two populations of UCN diverge in their behaviors. Separated by their relative energy these two populations are referred to as the fast and slow neutrons. The distribution of these populations is determined by the initial energy spectrum. Fast neutrons tend to interact with surfaces more often and in the Fermi model have a higher chance of penetrating a surface and being lost within it. Slow neutrons interact fewer times and have a lower chance of penetrating surfaces. It is sometimes relevant to fit these two populations with separate lifetimes, as a double exponential decay.

It is important to note that the production of UCN within the source is highly variable, having high sensitivity to both proton beam intensity impinging on the spallation target and temperature fluctuations in the isopure helium inside the cryostat. Both beam and temperature are monitored as part of the data taking, but for the levels of precision required for this experiment it is vital to have a UCN monitor detector upstream of the components that one is testing to normalize the counts in the main detector. In all the storage and transmission TCN18 experiments there is a monitor detector directly outside of the shielding used to normalize UCN counts.

2.5 Types of UCN Detectors Used for TCN18 Experiments

The UCN source at TRIUMF uses two types of detectors for separate purposes within the experiment, the ^{3}He detector for the monitoring of UCN production in the source, and the ^{6}Li detector for measuring the transmitted UCN. The ^{3}He detector has a lower background, but also a lower efficiency. The ^{6}Li detector has a more significant background that is sensitive to radiation, which is more likely to be present closer to the shielding, but also a higher efficiency. Furthermore the ^{6}Li has the capacity to deal with higher count rates without pile-up. In the new UCN source this will be vital as higher count rates are expected. Thus the ^{6}Li detector is used to measure the transmitted UCN and the ^{3}He detector is used for monitoring.

2.5.1 Lithium-6 Detector

The ^{6}Li detector is composed of cerium activated scintillating acrylic glass doped with Li connected to photomultiplier tubes (PMTs). A model and a photo of the detector can be seen in Fig. 2.9.

This detector has been built specifically for UCN detection, with the specifications for efficiency and stability in mind. The Li glass is made as thin as possible in order to minimize the sensitivity to thermal neutrons and gamma-ray scintillation. The neutrons interact with the ^{6}Li within the glass in the following way:

$$^6\text{Li} + n \rightarrow \alpha(2.05\,\text{MeV}) + t(2.73\,\text{MeV}). \tag{2.6}$$

The absorption of the neutron by the ^{6}Li results in a decay to an α particle with energy 2.05 MeV and triton (t) with energy 2.73 MeV. The neutron capture cross section is of order 10^5 b [50]. In order to maximize the capture of the decay particles triton and α produced in this interaction, the

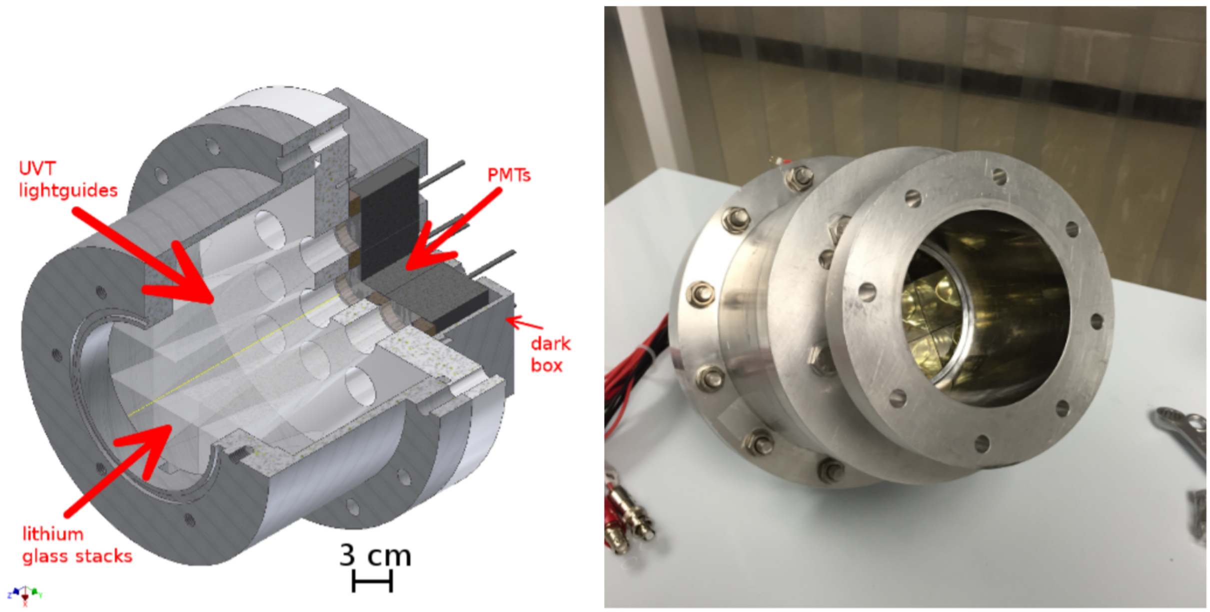

Figure 2.9: Model and picture of ^{6}Li Detector. The model shows the lithium glass stacks and the light guides, connected to the PMTs in the dark box. This is the model used in the simulations of the ^{6}Li detector. The front glass plane consists of two layers of glass, one which is ^{6}Li enriched and one which is ^{6}Li depleted. This layering improves the efficiency of the detector, as described in the text. All UCN absorbed in the second layer of the glass in the simulations are considered detected [50].

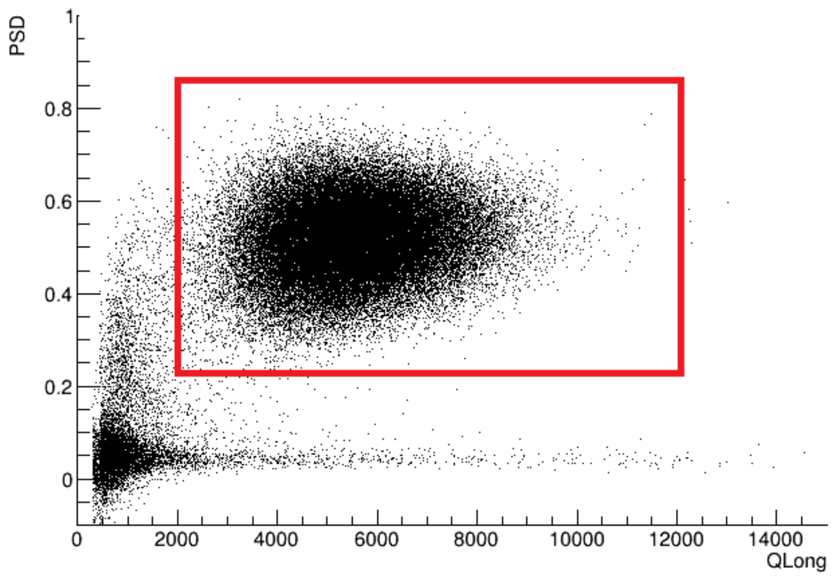

Figure 2.10: Example plot of counts within the ^{6}Li detector before cuts have been applied. The events which are within the UCN range have been outlined in red. The other events are background from gamma shine. Q_{L} is the long charge deposition of the signal in ADC units and PSD is a function of the long and short depositions as defined in Eqn. 2.7.

top surface of the scintillating glass is composed of two layers of material. The topmost is a 60 μm thick ^{6}Li depleted glass layer with a smaller capture cross section. The second layer is 120 μm thick ^{6}Li enriched glass [50]. Therefore, it is more likely that the neutron is absorbed in the second layer instead of the surface, thus both decay particles can contribute to scintillation light production and the signal proportional to the collected light becomes more significant.

Although it has a larger background from gamma-ray and thermal neutron interactions, the detailed information available from the energy deposition in the scintillator allows for filtering of events from UCN versus background. Thus cuts can be performed using pulse shape analysis, and an example of such a cut can be seen in Fig. 2.10.

Each time the detector is triggered the Pulse Shape Discrimination (PSD) software calculates two values, Q_{S} and Q_{L}, signifying the short and long charge deposition in ADC units respectively.

Depending on the particle event, the timing of the light deposition will be longer or shorter. These correspond to the sum of the signal below the baseline starting from 40 ADC units for Q_{S} and starting from 300 ADC units for Q_{L}. The PSD value is also calculated and defined as

$$PSD = \frac{Q_{\mathrm{L}} - Q_{\mathrm{S}}}{Q_{\mathrm{L}}}. \tag{2.7}$$

In Fig. 2.10 the PSD and Q_{L} have been plotted and a guide has been shown for where appropriate cuts at $Q_{\mathrm{L}} \geq 2000$ ADC units and $PSD \geq 0.2$ could be made to rule out non-UCN counts. These other events are mostly gamma depositions. Further detail of the pulse discrimination can be found in [50].

Ultimately the efficiency of the ^{6}Li detector is estimated to be $89.7^{+1.3}_{-1.9}\%$ [50]. The uncertainty mainly comes from uncertainty in the absorption in the ^{6}Li depleted layer. The detector is stable at 0.06% or better [50].

2.5.2 Helium-3 Detector

The ^{3}He detectors are gas proportional chambers, which operate using the avalanches of charged particles which deposit their charge on a wire within the chamber. The detectors used in the TUCAN experimental setups are UCN DUNia-10s, manufactured by AV Strelkob [51]. A model can be seen in Fig. 2.11. The chambers are cylindrical with a 50 mm length and 90 mm diameter entrance window. This entrance window is covered with a 0.1 mm foil of pure Al. The chamber is filled with a gas mixture. The filling of the chamber starts with an injection of ^{3}He gas to a pressure of 2.7×10^3 Pa followed by a mixture of 1% CH4 and 99% Ar up to 1.1×10^5 Pa. The resulting density of ^{3}He is expected to be 0.0044 kg/m^3. An anode wire is run in the radial direction of the chamber and a high voltage of 1.0 kV is applied to it [52].

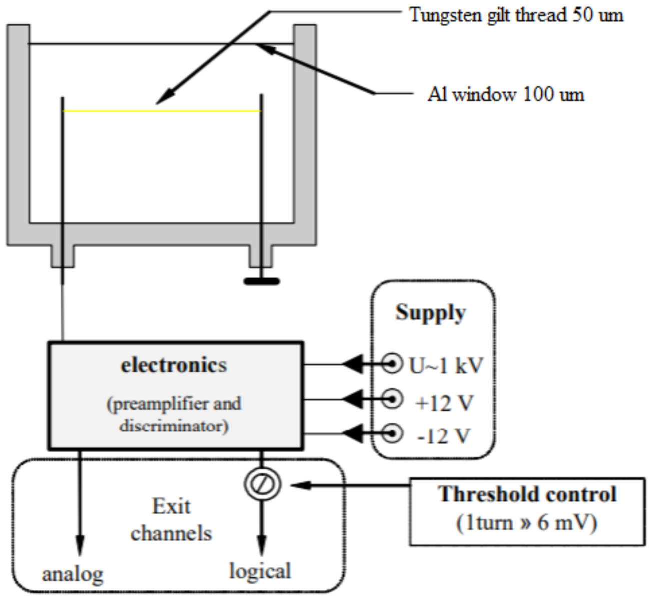

Figure 2.11: A schematic of the ^{3}He gas proportional chamber and electronics [51]. This chamber consists of a single Tungsten gilt wire with a 50 μm diameter, and an aluminum entrance window of approximately 100 μm thickness. The detector has an external threshold control [53].

The detector is sensitive to the slow neutrons stemming from the neutron source. The detection process happens via detection of the charged particle avalanche from the absorption of the neutron via the process:

$$^3\mathrm{He} + n \rightarrow t + p. \tag{2.8}$$

The detector efficiency can be evaluated by comparing the wavelength spectra for cold neutrons against the baseline ^{3}He proportional counter. More details of this process can be found in [52]. The efficiency of this detector was estimated by using λ as the neutron wavelength in nm as [52]:

$$\epsilon(\lambda) = 1 - e^{-0.100\lambda}. \tag{2.9}$$

By this estimate UCN on average would have a 74% detection efficiency in the ^{3}He detector [52].

CHAPTER 3

ANALYSIS OF DATA TAKEN IN THE 2018 RUN WITH THE VERTICAL UCN SOURCE CRYOSTAT PROTOTYPE

The following chapter is a discussion of analysis done on data which was recorded during the 2018 run of the TRIUMF UCN source. Throughout the fall of 2018 a variety of different measurements were done, primarily to characterize transport and storage efficiencies of components which will be used in the future nEDM experiment, as well as the characterization of the relative responses of the UCN detectors. This analysis includes the measurement of relative responses of the ^{6}Li and ^{3}He detectors, and analysis of the correlation between measurements taken of the proton beam from two instruments: the current measured by the cyclotron foil in combinations with the kicker rate, and a measurement taken using a beam current monitor on the proton beamline of the UCN facility.

3.1 Relative Responses of the ^{3}He and ^{6}Li Detectors

A direct measurement of the relative responses of the ^{3}He and the ^{6}Li detectors used in the TUCAN experiment has not been undertaken until this point. As the ^{3}He detector is used as a monitor detector in most experiments performed on the TUCAN setup, an exact number for the relative response is crucial for benchmarking simulations and a comparison to the expected efficiencies of the two detectors.

The experiments performed to measure these relative responses are referred to as TCN18-020 and TCN18-021. In this case there is no monitor detector, as the ^{3}He detector is one of the detectors being measured. At the time of these experiments the only two functional UCN detectors available within the TUCAN collaboration were the ^{6}Li and ^{3}He detectors. A model of the setup from UCN

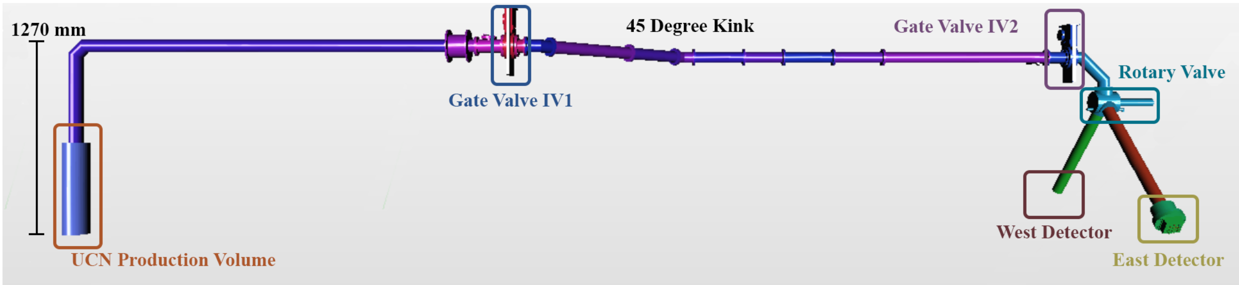

Figure 3.1: A model of the experimental setup during measurement runs of TCN18-020/TCN18-021 from the UCN source to the detectors. This model was used to simulate the experiment. The two gate valves are labelled in blue and purple in the figure. The rotary valve is shown on the right in light blue. The production volume is shown on the left in orange. The locations of the East and West detectors are shown in yellow and brown, respectively. The location of the 45 degree kink in the guide is labelled in black.

source to the two detector locations is shown in Fig. 3.1. In this model only one of the detectors is attached. In Fig. 3.2 the configurations of the two subsequent runs are shown, with TCN18-020 corresponding to run 898 and TCN18-021 corresponding to run 904. For run 898 each detector was run for 8 production periods. For run 904 each detector was run for 11 production periods. In the benchmarking simulations the valve is always sending UCN through the East guide with the detector attached. The simulation model includes only the guides with which the UCN interact.

The measurements of the relative responses were performed in two subsequent runs using the setup shown in Fig. 3.2. The flipping of the detector orientation was done in order to control for a possible asymmetry in the rotary valve, or a potentially higher background on one side of the configuration from gamma backgrounds, which could cause additional background counts in the ^{6}Li detector. In each of these runs UCN were delivered to the ^{3}He and ^{6}Li detectors in alternating production periods. It is assumed that there is a relatively constant temperature within the UCN production volume of the UCN source cryostat. Given this source stability, the ratio of the rates in the ^{3}He and ^{6}Li detectors normalized to the proton beam current delivered in each shot should be proportional to the ratio of their efficiencies.

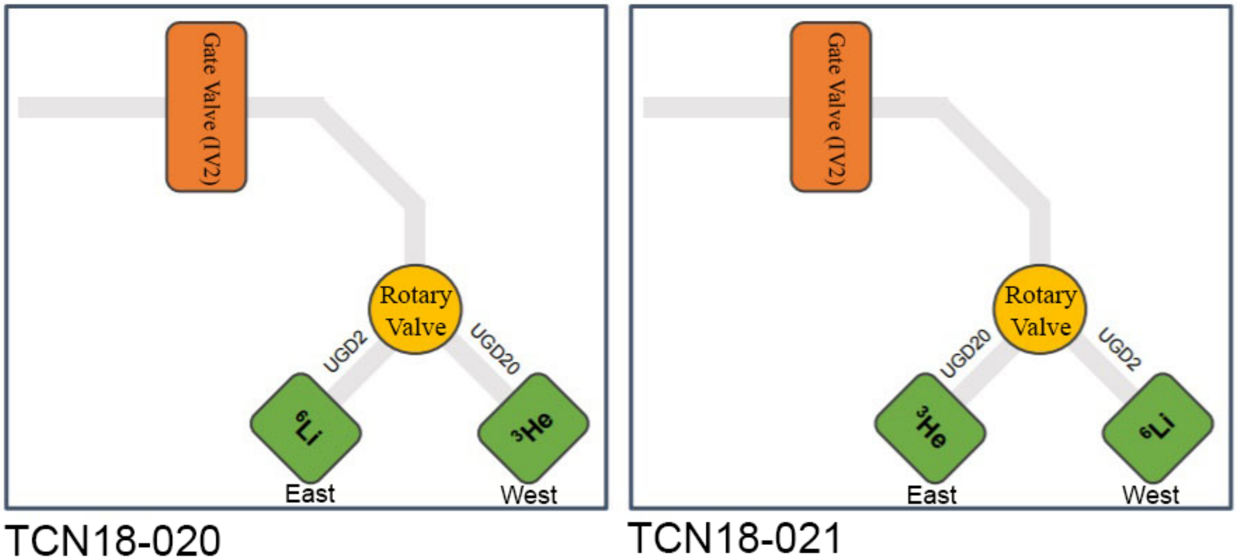

Figure 3.2: Configuration for the 898 and 904 runs of the 2018 TUCAN experiments. These correspond to TCN18-020 and TCN18-021, respectively. The two experiments are identical except for the exchange of the East to West location of the detectors and their associated guides UGD02 and UGD20 for the ^{6}Li and ^{3}He detectors, respectively. IV2 is a gate valve which can be opened after production. The rotary valve is switched to direct the UCN East or West, which takes a couple of seconds.

3.1.1 Calculating The Efficiency Ratio

For each production period the counts in both detectors between the time at which the valve is opened and the end of the run are summed. One run consists of many measurement cycles run with the same timing and experimental setup. A single cycle consists of an initial 60 s UCN production period at the beginning, during which the proton beam current is irradiating the target, and UCN are being produced in the isopure He volume. During this time IV2 is closed and IV1 is open. This means UCN are produced within the superfluid helium and a density of UCN is accumulated in the helium and the adjacent UCN guide volume. In this case the volume is open up to IV2. After the irradiation period IV2 is opened, allowing the UCN to travel through the guides toward one of the detectors, dependent on the setting of the rotary valve. The UCN are counted for 120 s, which is the counting window. Following, the background rate is measured for 10 s

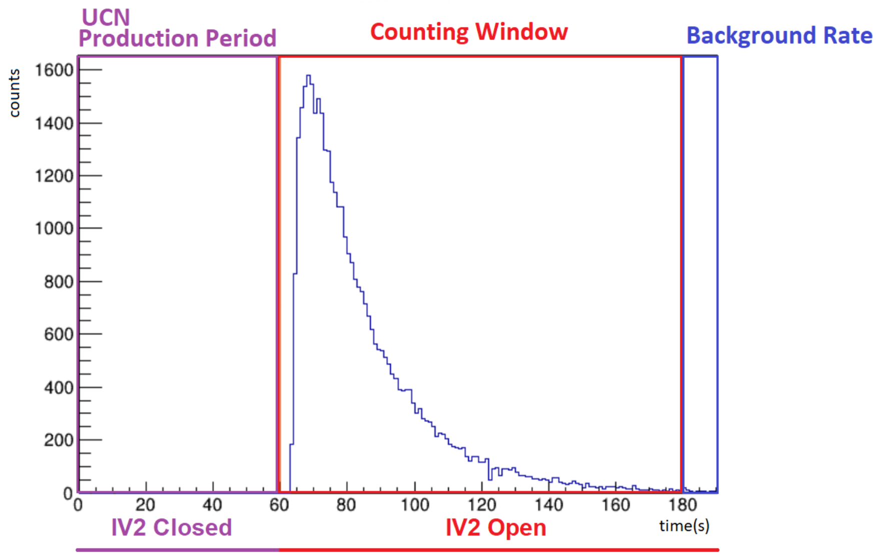

Figure 3.3: An example of the counts in the ^{3}He detector during a typical cycle of TCN18-020. During the first 60 s IV2 is closed, then it remains open for the rest of the cycle, closing at the end before the next irradiation starts. For the analysis only the counts between 60 s and 180 s are considered for the final summation of counts in the detector. This period, indicated with red lines, is called the counting window.

with IV2 open before the next cycle begins. For the detector which is not connected to the source through the rotary valve the counts are zero or near to zero. This was verified in the analysis, within uncertainty. The counts in the detector which the rotary valve is turned towards are used to calculate the efficiency ratios. An example of a typical count spectrum of the ^{3}He detector during a single production period can be seen in Fig. 3.3. The total number of counts for a single production period is determined by summing the counts in the detector between the time when the IV2 opens and the end of the counting period when all of the produced UCN have been detected or lost. This is called the counting window.

The total counts for each detector in a run were determined by summing over all counts in the counting window of the cycle and subtracting the background rate as determined by the average rate during the last 10 s of the cycle, shown in Eqn. 3.1. The last 10 s is used as the background because there is an additional background during the first 60 s from thermal neutrons produced during irradiation that have not been converted into UCN. The statistical uncertainty of this background rate is then taken to be $\sqrt{r}$, and added in quadrature to the total uncertainty of the counts. The counts were normalized to the mean proton beam current on target. It is assumed that the number of UCN produced is linearly proportional to the proton beam current on target, therefore dividing the counts by the average beam current during the production period for each cycle should account for beam fluctuations between runs. The total counts per cycle are then defined as:

$$C_{\text{total}} = \sum_{\Delta t}(c) - r \times 120 \text{ s}. \tag{3.1}$$

C_{total} is the total UCN counts for the cycle, c is the counts in the detector, Δt is the counting window, and r is the background rate as determined by the average counts in the detector in the last 10 s of the cycle.

In TCN18-020 and TCN18-021 the rotary valve was opened to the ^{6}Li and ^{3}He detectors in alternating cycles. For run 898 each detector was run for 8 cycles. For run 904 each detector was run for 11 cycles. The relative response of the two detectors is taken as the ratio of the counts in the ^{3}He detector in one cycle to the counts in the ^{6}Li detector in the next cycle as

$$\text{ratio} = C_{^3\text{He}(i)}/C_{^6\text{Li}(i+1)}. \tag{3.2}$$

$C_{^3\text{He}}$ is the UCN counts in the ^{3}He detector for a given cycle i, and $C_{^6\text{Li}}$ is the UCN counts in the ^{6}Li detector for the next cycle $i+1$. The ratio for each run was calculated using three different methods: A constant fit to the ratios over cycle order, a linear fit to the ratios over cycle order, and an average of all the ratios in the run. These fits were performed using MIGRAD from the analysis framework Root [54]. The constant fit is of the form

$$C_{\text{ratio const}}(t) = p_0, \tag{3.3}$$

in which the p_0 is a free parameter representing the ratio of detector counts and t is the order in which the production period took place. The linear fit is of the form

$$C_{\text{ratio lin}}(t) = p_0 + p_1 \times t, \tag{3.4}$$

where p_1 is the free parameter specifying the trend of the counts over the sequential production periods. The linear fit was used in case there was a slight linear trend due to temperature dependencies in the UCN source.

The average is calculated as

$$\langle \text{ratio fit} \rangle = \frac{2}{N} \sum_{i=1}^{N/2} C_{^3\text{He}(2i-1)} / C_{^6\text{Li}(2i)}, \tag{3.5}$$

where N is the number of cycles in the run and i is a specific cycle in the run. For the average both the statistical uncertainty from the initial measurement and the standard deviation contribute to the total uncertainty. The statistical uncertainty goes as $\sqrt{C_{\text{ratio}}}$. The fit introduces an additional uncertainty which goes as the standard deviation of the fit. The final uncertainty is a combination of these two contributions.

A slight linear trend was seen in the ratio of run 898. In order to determine the source of this trend the same fits described in Eqn. 3.4 and Eqn. 3.3 were applied to the counts in the ^{3}He and ^{6}Li detectors separately. A summary of the fits for both the ^{3}He and ^{6}Li detectors can be found in Tab. 3.1, as well as the average of the total counts for each detector in each run. The χ^2/DOF is also provided as a gauge of the goodness of the fit, where DOF is the degrees of freedom. The values for each individual method are compared. The ratios calculated from these methods are shown in Fig. 3.4. The counts for the 904 run are consistent over the different fitting methods. The slope of the linear fit for the 898 was then shown to be significant, as the uncertainty on the linear fit was less than the slope of the trend. This linear trend could be due to temperature effects. A further

Fit	Parameter	^{3}He		^{6}Li	
		Run 898	Run 904	Run 898	Run 904
Constant	p_0	38630 ± 74	39660 ± 63	61350 ± 88	58970 ± 77
	χ^2/DOF	3.59	1.25	2.63	3.08
Linear	p_0	38120 ± 166	39780 ± 126	61260 ± 176	59100 ± 166
	p_1	64 ± 20	-12 ± 11	12 ± 19	-11 ± 13
	χ^2/DOF	1.96	0.15	2.63	3.38
Average	average	38610 ± 489	39660 ± 356	61350 ± 559	58980 ± 59
	standard deviation	328	211	352	385
	statistical uncertainty	160	145	207	207

Table 3.1: A table summarizing results of the analysis of the UCN counts in the ^{3}He and ^{6}Li detectors in the 898 and 904 runs of the 2018 TUCAN experiment. These averages and fits were performed on background subtracted and beam current normalized data. The parameters for the fit are as defined by Eqn. 3.4 and Eqn. 3.3. The goodness of the fit is given by the χ^2/DOF value provided for both fits. For the average both the contributions to uncertainty from the standard deviation and from the statistical uncertainty are given.

discussion of this trend and its potential impact on the analysis can be found in Section 3.1.2. For the purposes of this analysis it was decided that this trend was minimal and that the effects averaged out.

The average total count for each of the detectors for each of the runs was also calculated. These averages were used to determine the ratio of the ^{3}He counts to ^{6}Li counts for each run. This resulted in the ratios shown in Fig. 3.4. There is a significant difference in the ratios between the two runs. Temperature and pressure within the UCN source during the production period of these two runs were not significantly different thus this has been excluded as potential systematic effect in this measurement, as discussed in Section 3.1.2. A comparison of the gamma counts in the ^{6}Li detector reveals that there does not appear to be additional radiation in one orientation as opposed to the other, which would affect the ^{6}Li count rate the most.

The gamma count rate per cycle was determined by counting the events in the ^{6}Li detector that fall outside of the cuts determined by the PSD and Q_{L} readouts which define regions of UCN counts, as discussed in Section 2.5.1. As with the UCN counts in the ^{6}Li detector, the total counts

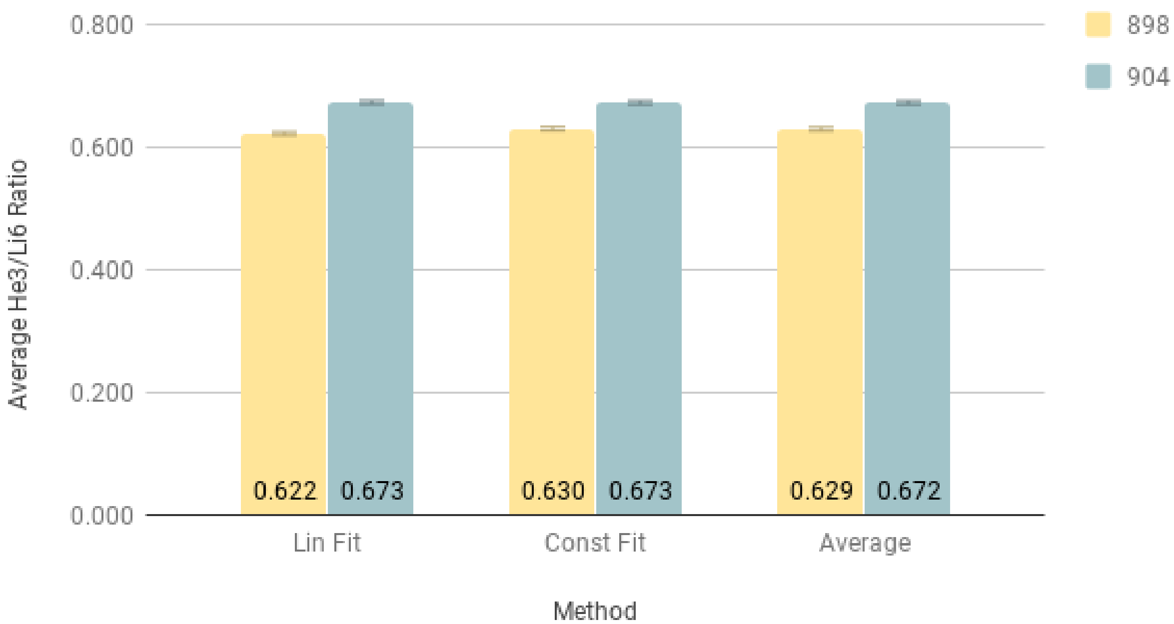

Figure 3.4: A summary of the relative detector efficiencies for the linear fit, constant fit, and average of runs 898 and 904. Across all the fits the ratio of run 904 is higher than that of run 898. This implies a systematic effect, which is most likely from the rotary valve, as described in the text.

Unit	Fit	^{6}Li Detector	
		898	904
Gamma Counts ^{6}Li Runs	Average	8460 ± 73	8560 ± 111
Gamma Counts ^{3}He Runs	Average	5020 ± 124	4891 ± 110

Table 3.2: A comparison of the gamma counts in the ^{6}Li detector between run 898 and run 904, where the gamma counts are defined as the region in which PSD is less than 0.2 and Q_{L} is less than 2000 ns . The discussion of these values can be found in Section 2.5.1. The counts are divided into counts for the cycles in which the rotary valve is open to the ^{6}Li detector and those in which it is not. Between the two runs the gamma counts are within the uncertainty of each other.

were averaged over the entirety of a run, and the 898 and 904 runs were compared for cycles in which the rotary valve was open to the ^{6}Li detector and for those in which the valve was turned the other way. A summary of these counts is shown in Tab. 3.2 and no significant variance is seen between the two runs. This indicates that the background radiation in the East to West configuration is symmetric.

The observed asymmetry in the efficiency ratio between run 898 and 904 and a lack of significant changes in corresponding temperature and pressure in the UCN source during the run indicates that there is an asymmetry in the rotary valve itself. Thus, one can probe the true ratio of the detector efficiencies in two ways; one can take the average of the ratio for the two runs, or the ratio of the detectors on the same side of the configuration. By dividing the average counts in the ^{3}He detector in run 898 by the counts in run 904 one gets the normalization factor N_{He}. By the opposite procedure on the ^{6}Li detector one can get the normalization factor N_{Li}. Ultimately, the normalization of the detectors to themselves on opposite sides gives $N_{\mathrm{He}} = 97 \pm 4\%$ and $N_{\mathrm{Li}} = 96 \pm 4\%$, showing a clear and consistent asymmetry in the rotary valve. Finally an average of the two ratios of ^{3}He:^{6}Li is given by:

$$(^3\mathrm{He}:\ ^6\mathrm{Li})_{\mathrm{final}} = 65.2 \pm 0.1\%. \tag{3.6}$$

This ratio will be used to properly benchmark simulations of TUCAN transmission and storage lifetime experiments. The relative counts of the ^{3}He and the ^{6}Li detector provide crucial information for transmission experiments.

3.1.2 TCN18-020/021 Temperature Drift and Dependence

In order to confirm that the temperature trends in run 898 did not have a significant effect on the ratio calculations, additional analysis was done comparing the trend in the ratio to the trend in the temperature. Several temperature sensors and two pressure sensors were attached to the relevant volume for production and detection. The pressure sensors are more stable and are trusted over the temperature sensors in the analysis, and the pressure can be easily converted to a temperature reading [55]. The pressure is measured in two pressure gauges for low and high pressures, referred to as pg9l and pg9h respectively.The ratio trend for the ^{3}He detector and ^{6}Li detector is shown in Fig. 3.5.

This trend does correspond to a slight temperature trend measured in the source as can be seen in Fig. 3.6. However, the total change in pressure seen over the course of run 898 is close to the total change seen in run 904. Therefore the contributions of these temperature effects should be comparable between the two runs.

In this analysis it was also found that there was a significant difference between the temperature during the ^{3}He and ^{6}Li cycles. This is due to the additional pumping power introduced into the system by a vacuum pump which is attached to the ^{6}Li detector with the purpose of reducing outgassing of the scintillation and light guide materials. As a consequence, the pressure and thus the temperature in the UCN source volume is lowered during the ^{6}Li runs. Ultimately, The difference in temperature is not significant as it is within the uncertainty of the thermometers and additionally it is not large enough to explain the observed effect on UCN count rate.

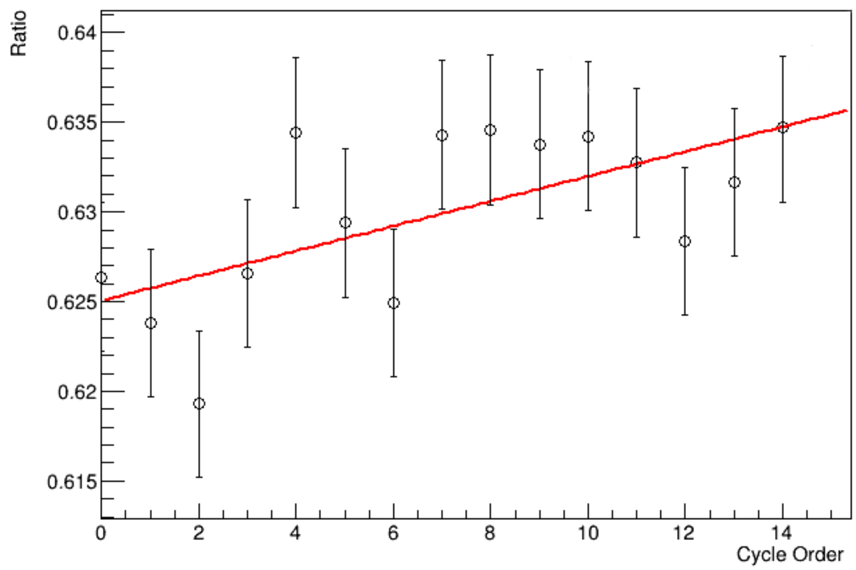

Figure 3.5: Trend of ^{3}He: ^{6}Li over time in run 898. This data is fit with a linear fit with constant p_0 and a slope p_1. A slight linear trend can be seen, due to a slight linear trend seen in the ^{3}He detector in 898, as can be seen in Tab. 3.1.

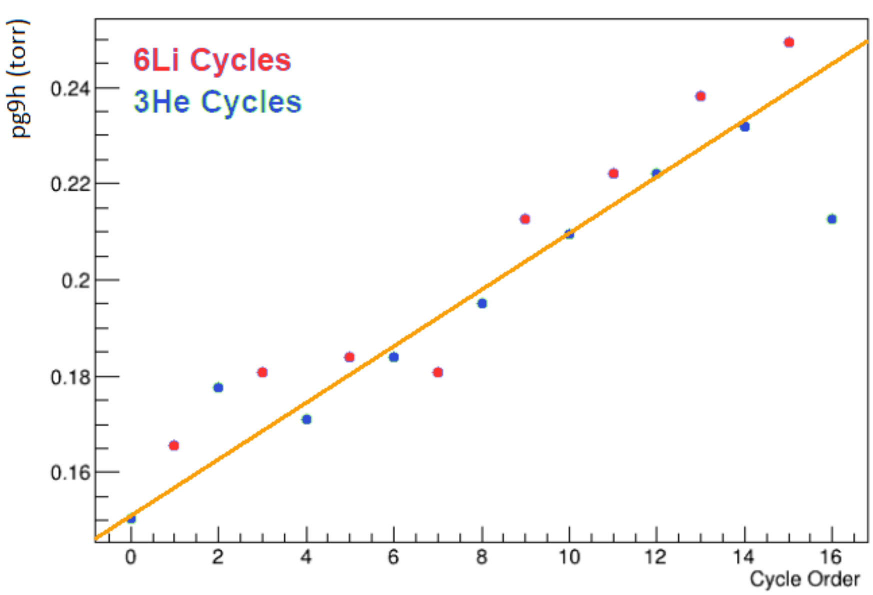

Figure 3.6: Trend of pressure measured over time in run 898, as measured in the pressure gauge pg9h. The pressure increases over the course of this run. Cycles with the rotary valve pointed towards the ^{3}He detector and the ^{6}Li are shown in blue and red, respectively. An orange line has been drawn to indicate the upward trend of the pressure.

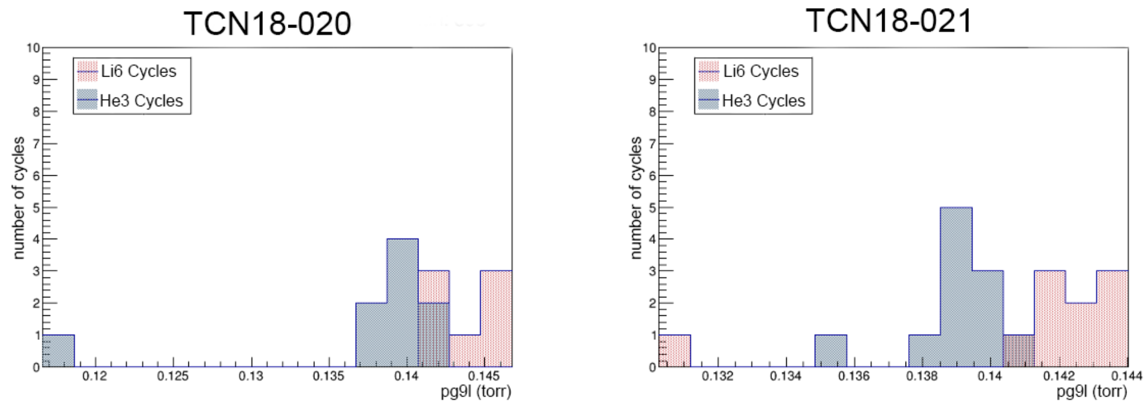

Figure 3.7: Comparison of the average pressure during the 60 s irradiation period at the beginning of each cycle for both run 898 and run 904. In red is are the ^{6}Li cycles and in red are the ^{3}He cycles. It is clear that the pressure in the ^{6}Li cycles is always higher. This is due to the additional pumping which the system experiences at the end of the ^{6}Li cycles, which means the pressure through the ^{3}He cycles is lower.

3.1.3 Simulations of Experiments TCN18-020 and TCN18-021

In order to create a quantitative benchmark for the detector efficiencies to be used in future simulations, models of TCN18-020 and TCN18-021 must be produced and the experiment must be reproduced in simulation. The ratio between counts in the ^{3}He detector and ^{6}Li detector in simulations will be compared to the one determined by experiment. The simulation is run with the timing parameters described in Section 3.1.1. The model used is the one in Fig. 3.1, with only one orientation of the rotary valve.

The simulations of TCN18-020 and TCN18-021 were run using the model introduced in Fig. 3.1, with polished steel being the default material. The production volume has a nickle phosphorus coating. There are also two copper gaskets and one O-ring made of Viton which is visible to the UCN within the simulation. The light guides within the ^{6}Li detector are acrylic and the top has both the ^{6}Li depleted and ^{6}Li doped layer. All UCN which are absorbed in the ^{6}Li doped layer or the light guides are considered detected by the ^{6}Li detector. The ^{3}He detector contains an absorbing plate beneath an aluminium foil. All UCN absorbed in this plate are considered detected by the ^{3}He detector. The rotary valve's internal shape is square, visible in Fig. 3.8, whereas all the

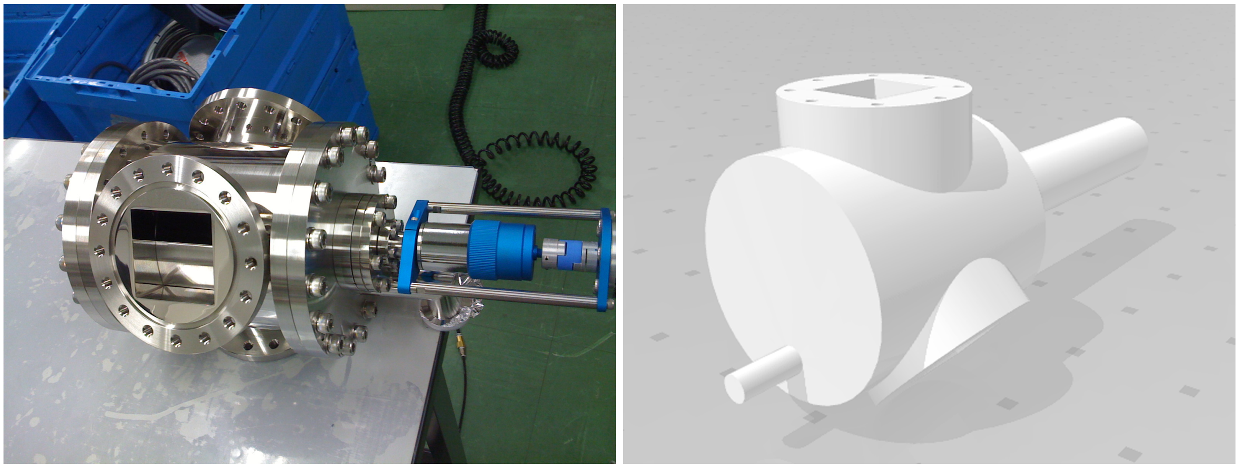

Figure 3.8: Side by side comparison of the rotary valve used in the TCN18-020 on the left and TCN18-021 and the simulation model on the right. The guide within the rotary valve is square, which makes the connection between the valve and the cylindrical guides a high loss surface. The model shown on the right only directs UCN in one direction.

other guides are cylindrical. Transition between these two different shapes makes the entrance of the rotary valve a high loss zone.

In the TCN18-020 and TCN18-021 simulations the production period was 60 s long which corresponds to the irradiation period at the TRIUMF source. UCN are produced with a square root energy spectrum between 0 and 300 neV. During this period IV2 remains closed. After this 60 s irradiation all the valves are opened and the counting period begins.

For each detector 10^6 particles were simulated. The counts in the ^{3}He detector are divided by the counts in the ^{6}Li detector. This gives a ratio of ^{3}He:^{6}Li of $80.7 \pm 0.4\%$. Thus, it is clearly necessary to adjust the efficiencies of the simulated detectors. Of the two models the ^{6}Li detector is more refined, as it includes a model of the two layers of depleted and doped Li glass, as well as the PMTs, described in Section 2.5.1. The ^{3}He gas proportional chamber is simply modeled as a black absorber, which is likely to be inaccurate. For the simulation done in this thesis and other related work the efficiency of the ^{3}He detector is adjusted by a factor of 80.9%, which is the value determined by taking the ratio of the measured relative responses of the ^{6}Li and ^{3}He detectors over the simulated ones. This means that in future simulations the relative counts in the two detectors should more closely reflect experimental results.

3.2 Measuring the Proton Beam Current on the Spallation Target of the UCN Facility

The proton beam from TRIUMF's main cyclotron is directed onto the spallation target of the UCN facility to create free neutrons. The flux of neutrons towards the moderators and converters of the UCN source is approximately proportional to the proton beam current. A larger proton beam current will create more neutrons, thus more UCN. However, this also increases the heatload on the target and UCN source, as well as secondary radiation. The intensity of secondary radiation impacts radioactive activation of all materials in and around the target and source, as well as the radiation level in the experimental areas in the meson hall. The heatload and radiation must be managed in order to protect the equipment and maintain safety standards.

First, the proton beam current is an important parameter used to normalize the measured UCN counts, as described in the previous section. Second, the requirements for radiation protection are directly affected by the proton beam current. The UCN target itself is specified for use up to 40 μA. Therefore, the beam needs to be tripped by a fast interlock to protect the equipment in case the current becomes too high. If the current exceeds the accepted limit the target and other structures would be irradiated and the activation levels of the materials would rise, potentially causing damage to the target and in the worst case this radiation could even destroy the target. In the current configuration, the UCN source prototype can only handle a heatload of 1 μA in stable operational condition. Additionally, the biological radiation shielding has been designed to accommodate this heatload and approved by the Canadian Nuclear Safety Commission (CNSC) for proton beam currents of up to 1 μA. A higher beam current would cause increased radiation levels in the experimental areas in the meson hall. Thus, another interlock is implemented in order to trip the proton beam if it exceeds 1 μA. The proton beam current can be adjusted by using the kicker magnet and adjusting the duty cycle. Knowing the amount of proton beam hitting the target is important for several reasons. Given that the beam on target consists of single 120 μA pulses of 1 ms, averaging over different time scales is necessary. The average values over those different timescales need to be fed into the different interlocks, as well as being recorded with other important UCN source operation parameters so that the beam current is always well defined and known. The cumulative total proton beam current on target is also an important parameter because it allows to compare measured activation levels of the target and other components to values found by calculations or simulations for benchmarking processes. In this section the amount of proton beam on target during the 2018 run is analyzed, as well as the behavior of the beam monitoring devices for the interlocks and how well their measurements correlate.

3.2.1 Total Beam Current on Target in 2018

The most precise measurement of the proton beam current delivered towards the UCN source comes from a combination of the current measurement in the cyclotron foil and the kicker magnet described in Section 2.1 which directs proton beam bunches between BL1U and BL1A. The initial proton beam current is measured at the stripper foils in the cyclotron. The kicker magnet determines the fraction of proton pulses it is directing towards BL1U. From this the predicted proton beam current at the UCN target can be determined. Measurements from the kicker and cyclotron foil are used to determine the total beam current on target. A similar analysis was also done for the TUCAN experimental runs performed in the fall of 2017 by the TUCAN collaboration. In order to determine if higher current loads are changing the behavior of the target, it is important to monitor the total beam current over the course of all TUCAN runs. There is an additional beam monitoring device closer to the source which is used to trigger interlocks in the case that too much beam is being delivered to the target. It can be seen in the bottom of Fig. 2.3 as 1UTNIM2. For the purposes of this discussion it will be referred to as TNIM2.

The total beam on target was calculated by summing the instantaneous current measurements from the kicker magnet over the entirety of the run. Between the measurements in 2017 and 2018 the beam current logging system was changed. Previously the beam current had only been stored for times in which the kicker magnet was kicking. Following the change from 2018 onward the beam current was stored for both times that the kicker magnet was on and directing beam towards the UCN target as well as when the kicker was off and the UCN target was receiving no beam. The kicker magnet is turned off during periods in which no beam is required for UCN production, or when modifications are being made in the experimental area.

Due to the changes in logging the analysis method to determine the total beam on target needed to be reconfigured. Fig. 3.9 is a graph of the current over the whole run, with the measurements for the times the kicker was on being shown in green, and the measurements for the times the kicker was off being shown in red. In order to calculate the total current on target only the current readings in green are summed.

After carefully ensuring that the analysis mechanism takes into account the changes in the DAQ system correctly the final total beam on target for the 2018 run was 65.6 ± 0.1 μAh, which is calculated from the predicted current at the kicker magnet. For reference, the 2017 run had 39.1 ± 0.2 μAh delivered on target.

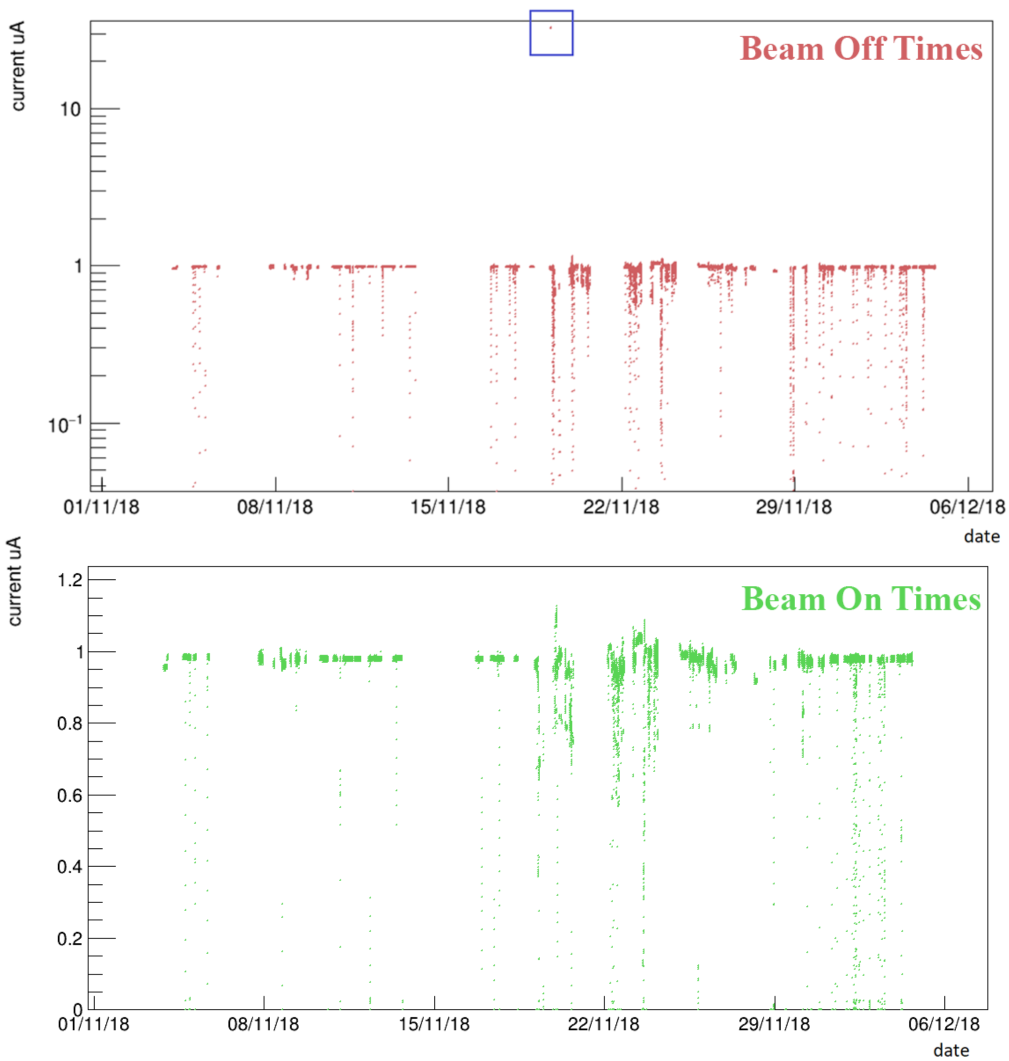

Figure 3.9: Predicted current determined by the kicker magnet over the 2018 UCN run. The points are separated into times at which the kicker magnet was on and delivering beam to the UCN target, shown in green on the bottom, and times when the kicker magnet was turned off and no beam was being delivered to the UCN target shown in red on the top. Only the values in green were used to calculate the total current. A significant outlier in the beam off target time is outlined in blue, where the kicker fractions were being scanned during a period when the kicker magnet was not turned on. This would have tripped the interlocks if the beam had been on target.

3.2.2 Investigating the Correlation of the Toroidal Non-Intercepting Monitor Readout to the Predicted Beam Current

During the 2018 TUCAN experimental run the beam was operated mostly at low current, where the proton beam current was in the range of 1 μA. In the low current ranges the chances that a fluctuation in the beam will bring the current above the damage threshold of the target is small. However, for the production runs in the future the TUCAN Collaboration aims to increase the proton beam on target to 40 μA. It is necessary to ensure that the accuracy of the monitoring of the proton current is well understood for the interlock and thus machine protection.

As discussed, there are effectively two methods by which the beam on target is monitored. The measurement from kicker magnet and cyclotron foil will be referred to as the predicted current in this section. In addition to this predicted value there are several beam monitors as mentioned previously, and listed in Tab. 2.1. These monitors required calibration and may drift during operation. Ideally the predicted current and induced current measurements read out by beamline components of the beam delivered to the UCN target should have a 1:1 correlation. The beam monitors used in the UCN experimental area are toroidal non-intercepting monitors.

Toroidal Non-Intercepting Monitor

The beam monitor used to measure the proton beam current is a Toroidal Non-Intercepting Monitor (TNIM). The particular TNIM referenced in this analysis is TNIM2, located downstream of the kicker magnet and separated from the target by a harp and a collimator, as can be seen in Fig. 2.3. The TNIM2 serves as the interlock signal during BL1U operation, triggering on currents greater than 1 μA. This monitor is key, as it is used as an interlock during beam delivery to ensure the beam current does not exceed licence or safety limits. If the reading in TNIM2 exceeds the accept-

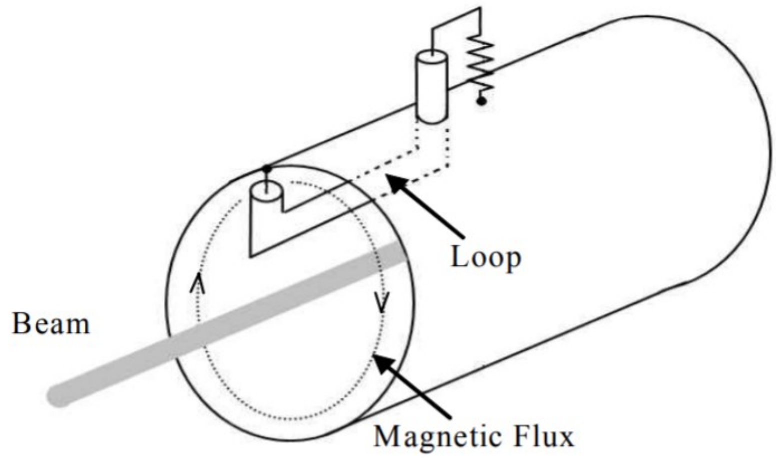

Figure 3.10: A schematic of a commonly used beam monitor. The beam, shown in grey, passes through the toroid, inducing a magnetic flux which in turn induces a current in the loop. This current is then measured [56].

able value it will trip the cyclotron to prevent damage to the target. As illustrated in Fig. 3.10, the detector works via measuring induced current from the passage of the beam through a toroid. The current passing through the toroid produces a magnetic flux in the loop. This in turn generates a current which is measured [56].

The electronics of the TNIM2 had been updated at the beginning of the 2018 run, as the previous electronic setup had significant drifts and an offset that needed to be manually reconfigured. This change was not fully implemented until after November 9th, 2018. As can be seen in Fig. 3.11, there is an initial period in which TNIM2 only provided unphysical readings.

After TNIM2 was configured properly, the readings became linear and proportional to the beam during periods in which the kicker magnet was kicking. After the end of the beam time, when no beam is passing through the TNIM2, a general drift in the reading can be seen over time in Fig. 3.11. A green line has been drawn to highlight this drift. Additionally, a beam tuning period in late December can be seen as a brief jump in the reading.

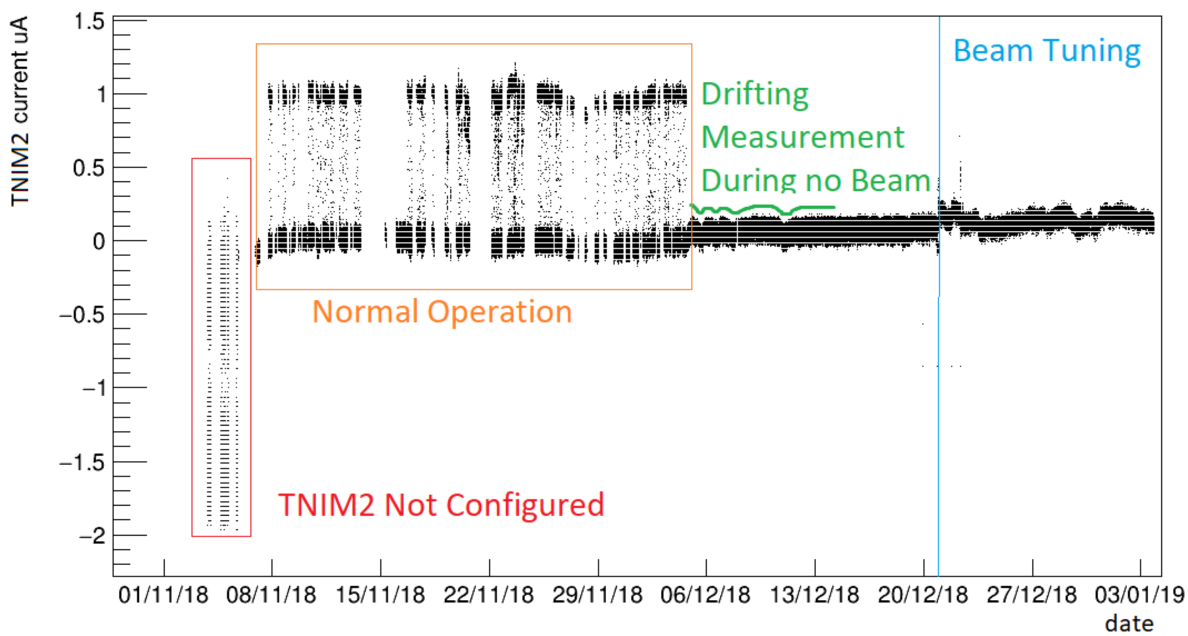

Figure 3.11: The TNIM2 reading for the 2018 run. In the red box the period in which TNIM2 was improperly configured is shown. The beam on target times can be seen in orange and the measured current is approximately 1 μA. In the no beam period that occurs after 04/12/18 a green line tracing the drift of the measurement is shown. Finally, the blue vertical line is the time at which some beam tuning occurred, therefore there was beam on target separate from the normal operation.

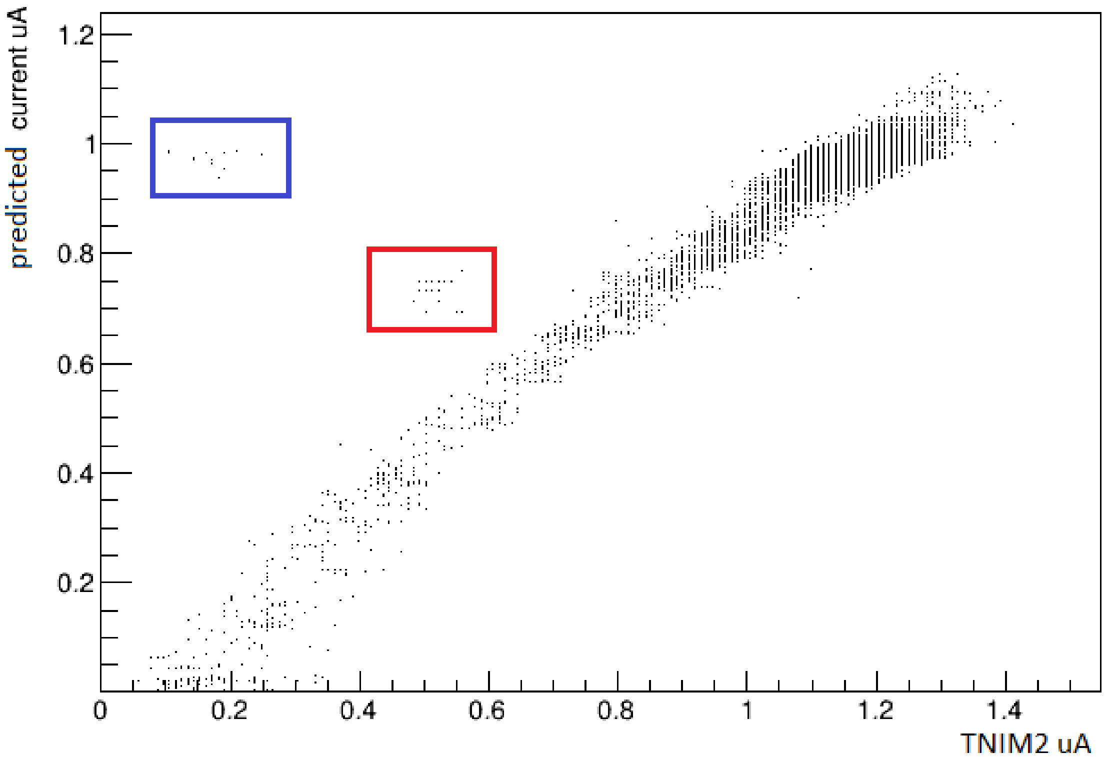

Figure 3.12: Plot of the TNIM2 readings against the predicted current for the 2018 run cut on periods in which the electronics were configured properly, the beam was on target, and dropping the first and last reading from every beam on period to account for averaging errors. A positive 0.2 μA offset is introduced into the TNIM2 data in order to keep all the values positive for analysis. Outliers at high currents are outlined in blue and red. These two regions correspond to nonstandard beam operation times outlined in red, and an unexplained outlier outlined in blue.

At this point it is interesting to consider the comparison of the predicted current with the TNIM2 reading. In Fig. 3.12 the readings are plotted against each other, after applying some cuts. Only readings where the electronics were configured properly, the beam was on target, and it was not the first or last reading of the beam period are plotted. Additionally, a 0.2 μA offset is introduced into the TNIM2 data in order to keep all the values positive for the analysis.

Between the predicted current of 0.4 and 1 μA the ratio is linear. A spread can be seen, likely due to slight drifts in the TNIM2 reading. Below 0.4 μA, the spread of TNIM2 readings increases significantly. These non correlations occur mainly at low predicted currents, where the background in TNIM2 becomes more significant. There are some high current exceptions to this. If one defines the correlation (L) of the reading in TNIM2 and the predicted current to be

$$L = \frac{I_{\text{TNIM2}}}{I_{\text{predcur}}}, \tag{3.7}$$

with I_{TNIM2} as the current measured in TNIM2 and I_{predcur} as predicted current, then one can plot this correlation against the predicted current and observe where it diverges. The plot of the correlation against the predicted current is shown in Fig. 3.13, in which a clear spike appears at lower predicted currents. This indicates a divergence from the 1:1 correlation between the predicted current and the TNIM2 reading.

The change in the relationship between the predicted current and the TNIM2 reading at lower currents can be attributed to nonstandard operation of the beam. An example of this nonstandard operation which might affect the correlation between these measurements are times in which the cyclotron is ramping up or down. The TNIM2 measurement is not as precise for measuring rapidly fluctuating beam currents. In general, one would not be operating the source during periods in which the beam is ramping up or down. The clusters outlined in blue in Fig. 3.13 are times where the beam was ramping up or down during the operation of the UCN source. Thus, they can be excluded from the analysis. The points outlined in red were not during these times and will be addressed below. By plotting the ratio against the predicted current one can exclude additional outlying points.

By assuming that most operation in which the cyclotron foil was reading less than 50 μA is non-standard operation, which corresponds to predicted currents of 0.1 μA or less depending on the kick fraction, the outliers become limited to a single cluster in which the TNIM2 readings were significantly lower than the predicted current in a period of 2 hours on 26/11/2018, outlined in red

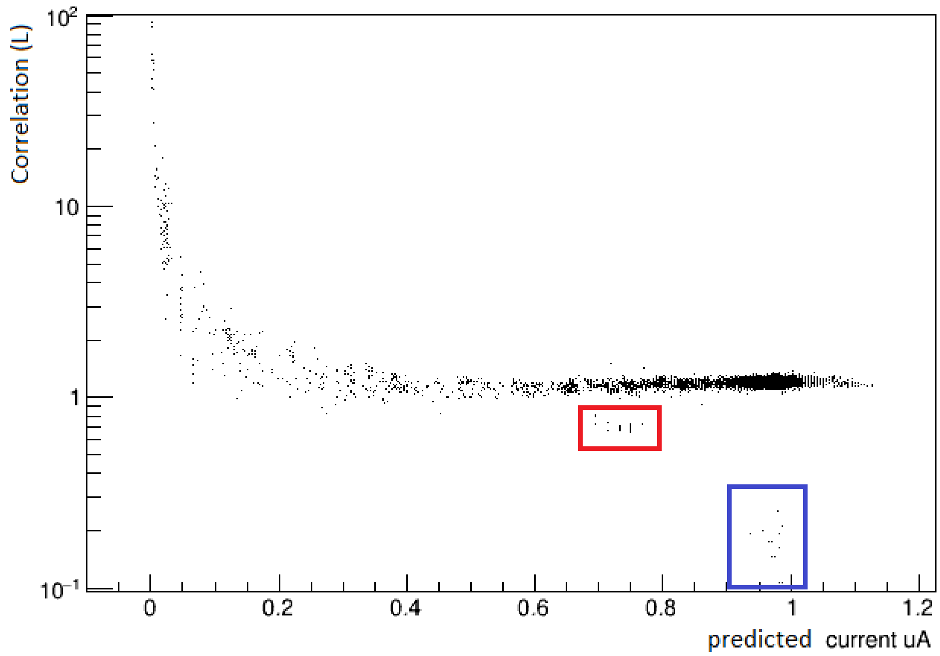

Figure 3.13: A plot of TNIM2 to predicted current readings against the predicted current value, showing how the correlation becomes worse at low current readings, but also showing the two regions in which the TNIM2 measurement poorly predicts the current, outlined in red and blue. These two regions correspond to nonstandard beam operation times outlined in red, and an unexplained outlier outlined in blue. This is also shown in Fig. 3.12.

in Fig. 3.13 and Fig. 3.11. This is an area in which future beam development runs will provide more insight into this behavior.

Ultimately the 2018 run has shown that for the regions of interest in the low current of approximately 1 μA operation of the proton beam readings from TNIM2 are sufficiently accurate to be used as an interlock trigger. It is clear that during measurements of currents below 0.2 μA the TNIM2 shows a nonlinear response, however, it is not necessary to trigger on currents in that range so this nonlinear response is not an issue for the purposes of the TUCAN collaboration or TRIUMF cyclotron machine protection. Further testing for the high current operation needs to be performed, in order to understand the few outliers found, but in normal operation the measurements from TNIM2 are sufficiently accurate to provide the interlock trigger required.

3.3 Correlation Between Daily Storage Lifetime and Monitor Counts

The number of UCN produced in the source should be a function of several of the parameters discussed previously, such as the proton beam intensity and temperature dependencies, as well as additional parameters including the storage lifetime of the UCN source and the scale of the volume available to the UCN during the production period. Throughout the 2018 run, daily measurements of the source storage lifetime were made to track the possible degradation of the UCN source over the course of the run. A full description of a storage lifetime measurement will be given in Chapter 4. However, for the purposes of the following discussion, it is sufficient to understand that the storage lifetime of the production volume τ corresponds to the quality of the surfaces and is proportional to the UCN production density. Therefore the counts in the monitor detector should be roughly proportional to the daily storage lifetime throughout the entire beamtime.

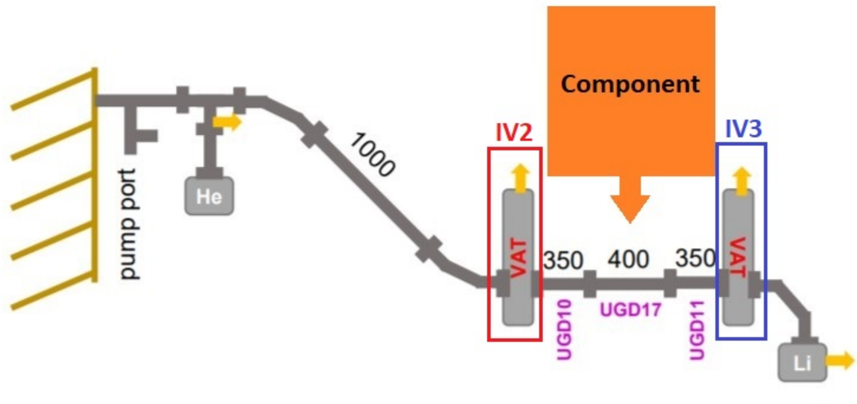

Figure 3.14: An example TUCAN experimental setup past the shielding elements. This diagram shows only the portion of the UCN facility outside of the radiation shielding. The valves IV2 and IV3 are marked in red and blue, respectively. The UCN counts are monitored in the ^{3}He detector, labelled He in the figure, and the final counts are measured in the ^{6}Li detector, labelled Li in the figure. In a typical storage or transmission measurement the component being tested would be placed in between the two valves, indicated by the orange box. The lengths of the example guides in mm are given in black above the guides.

If all other factors remain constant in the setup, one expects a direct proportionality between the counts in the monitor detector and the daily storage lifetime. Introducing new factors such as materials with different coatings and height changes should introduce an additional factor into this proportionality. In order to characterize the behavior of the UCN source storage in relation to the counts during the monitoring period of the ^{3}He detector, the daily source storage measurement was plotted against the monitor counts for the component characterization measurements.

During component storage lifetime measurements UCN were produced up to IV3 for the majority of the measurements, labelled IV3 in Fig. 3.14 excluding some setups in which there were only two valves in the setup and others in which different timings were being tested. Although the UCN are only produced in the isopure He volume, the additional volume connected to the source volume affects the production rate of the source. This is due to a combination of pressure effects and the material surfaces which the UCN are exposed to during the production. However, it seems that

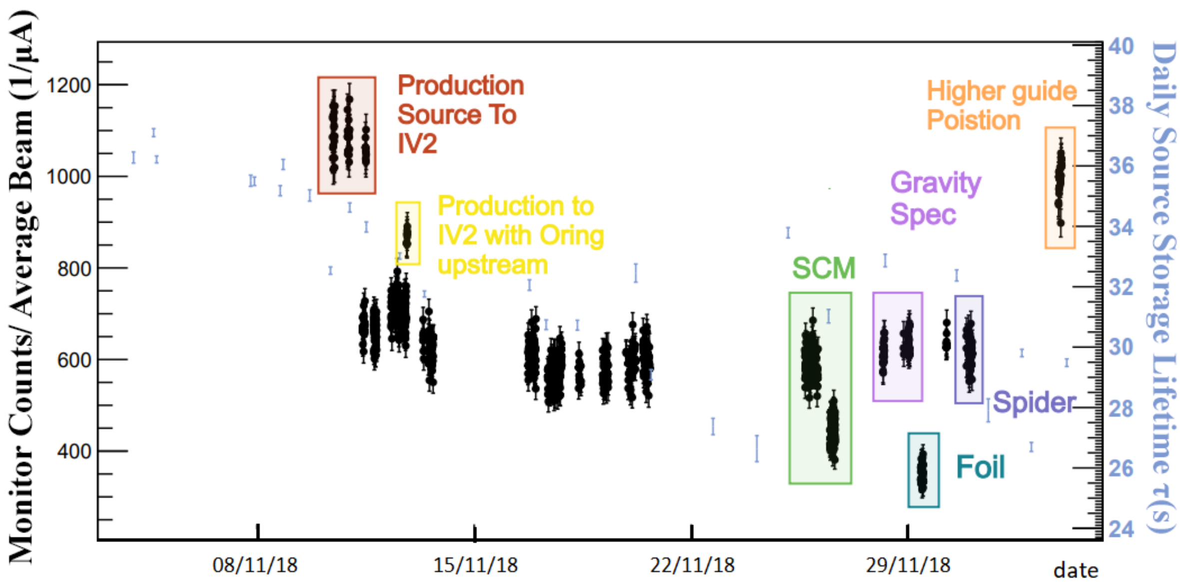

Figure 3.15: The counts in the ^{3}He monitor detector normalized to beam current over the course of the 2018 TUCAN run during the component storage measurements. The points in black are the ratios of the counts in the ^{3}He detector to the average beam during the irradiation period for all the TUCAN experiments run in 2018. In blue are the daily storage lifetimes ($\tau(s)$) of the UCN source, which should be proportional to the number of UCN produced. The labels denote experiments which were expected to significantly change the transmission to the ^{3}He detector. Details of these experiments can be found in the text.

although the characteristics of the volume in which the UCN were produced varied from run to run for the component storage lifetime, the monitor counts normalized to the beam current during the production roughly correspond to the daily UCN source storage measurements.

In order to sensibly compare the setups and understand how their geometry or surfaces might impact the daily storage measurements, they must be separated based on their lengths and other production limiting characteristics. As can be seen in Fig. 3.15, several configurations have been investigated:

1. Shown in red are experiments in which the volume available to UCN during production was smaller as IV2 was closed during production.

2. Shown in yellow is a measurement where the IV2 valve was flipped and the Viton O-Ring with a high UCN capture cross section was exposed to the volume in which the UCN are produced. UCN were only produced up to IV2. The cluster of black points below are the same setup, but with IV2 open.

3. Shown in between the yellow and green labels are experiments done in the same position, but testing guides with different coatings in the position of the orange box in Fig. 3.14. For this period the monitor counts have a roughly constant proportionality to the source storage lifetime.

4. Shown in green are experiments done with the superconducting magnet (SCM), which will be used in the future nEDM experiment. The location of the SCM is indicated by the orange box in Fig. 3.14.

5. Shown in blue are foil experiments that were done with a foil in front of the ^{3}He detector [57]. This foil is used to prevent contamination of the source volume. The foil reduced the number of counts in the monitor.

6. Shown in light purple are the experiments done with the gravity spectrometer. These exper-

iments were performed with IV2 open and IV3 removed.

7. Shown in dark purple are tests with a custom designed "spider" component being tested in the position indicated by the orange box in Fig. 3.14. This spider is an alternative to a burst disk in the setup. This experiment was done with a shorter distance between IV2 and IV3.

8. Shown in orange were experiments performed with a higher position guide. Higher guide position refers to when the guides were adjusted to have less of a drop between the production and detector, therefore significantly increasing the UCN counts in the monitor detector.

Overall, it can be concluded that, excluding the effect of the configurations with significant variations, the counts in the monitor detector roughly correspond to the measured storage lifetime of the UCN source. The precision of this correlation is difficult to quantify, and the storage lifetime will not be used to normalize UCN counts. However, the observed reasonable proportionality indicates that the TUCAN collaboration's understanding of the UCN source under different operational conditions is under control.

CHAPTER 4

SIMULATIONS OF THE ENERGY SPECTRUM OF THE VERTICAL UCN SOURCE CRYOSTAT PROTOTYPE

As discussed in Section. 2.2, the TUCAN collaboration has shipped and installed the vertical UCN source cryostat prototype from the Research Center for Nuclear Physics (RCNP) of the University of Osaka, Japan, to TRIUMF in Vancouver, Canada. This prototype UCN source has been characterized and optimized at RCNP [12] and has been operating at TRIUMF for approximately 1 month every year since 2017 [49]. The characterization at RCNP included a spectrum measurement of the produced UCN, since the energy of a UCN determines how it will interact with material surfaces.

The measurement at RCNP was performed using a gravity spectrometer with an adjustable UCN absorbing plate, which can be used to remove the higher end of the UCN energy spectrum before the UCN arrive at the detector. The analysis of this work is detailed in [31]. In a process described below, the shape of the UCN energy spectrum of the UCN source at RCNP was extracted. It could be assumed that the energy spectrum of the source has remained the same after the shipping and installation at TRIUMF, as differences in beam current and temperature mainly affect the number of UCN produced. However, it is possible that a change in quality of the surfaces of guides or even the UCN production volume itself has occurred, which could affect the final UCN energy spectrum produced. The coating on the production volume could have deteriorated over time or during shipping and installation. Additionally, some of the UCN guides have been changed from the setup at RCNP. Differences in the distance over which the UCN must travel between their production and detection could impact the spectrum as well, as the distance over which the UCN travel asymmetrically affects transmission of high energy and low energy UCN. With the guides having been changed since the measurement at RCNP, different Fermi potentials of the guides could result in the loss of different parts of energy spectrum during UCN transmission. Repeating the measurement of the UCN energy spectrum of the vertical source as it is currently installed at TRIUMF is important, to ensure that the UCN source, as well as the energy of the UCN produced within it, are well understood.

In order to estimate the amount of beam time a measurement of the energy spectrum would require at TRIUMF, simulations of the gravity spectrometer attached to the TRIUMF configuration must be performed. The first step in ensuring that this simulation is sensible, was to reproduce the spectrum experiment [31] at RCNP in the simulation software. A description of this initial simulation will follow below. The process of reproducing the measurements performed at RCNP in simulation proved difficult using the version of PENTrack which was available at the time of this analysis. The implementation of the UCN interactions with the surfaces of materials made it impossible to recreate the energy spectrum measured at RCNP. Ultimately, the spectrum measurement of the UCN source as installed at TRIUMF has not been performed, due to insufficient beamtime. The work done here helped confirm that the simulation software needed to be updated. Future iterations of these simulations could help benchmark how changes to the software improved the accuracy of the simulation.

In this chapter I will describe simulations of the vertical UCN source at TRIUMF, as well as the simulations of the spectrum measurement performed at RCNP. The results of these simulations will be fitted and analyzed alongside the data from the spectrum measurement performed at RCNP. The discrepancies in the energy spectra and the way in which the simulation software has been updated to reflect these discrepancies will be described.

4.1 Development of a Spectrum Bottle Experiment for Future Measurements at TRIUMF

At RCNP the UCN spectrum was measured using a gravity spectrometer. This gravity spectrometer is a cylindrical volume into which the UCN are filled from the bottom, with an absorbing plate attached to a vertically adjustable piston at the top of the bottle. By running a sequence of measurements of this chamber with the piston at various heights, the energy spectrum of the produced UCN may be extracted.

After moving the source to TRIUMF this is one of the experiments that should be repeated in order to understand how the difference in the surface quality of the source volume and guide quality may have affected the spectrum of the source. The planning of this experiment was preceded by simulations and analysis of the components to ascertain the time needed to obtain the appropriate statistics and set a baseline expectation for the storage lifetimes and spectrum. This estimation is not straightforward, as the changing plate height affects how many UCN arrive at the detector in a nonlinear way, and the quality of the guides and the distances that the UCN must travel also have significant contributions. Ultimately, the simulations of the gravity spectrometer revealed an inconsistency in the simulation software.

4.1.1 Spectrum Bottle

The gravity spectrometer used at RCNP is a stainless steel cylinder into which the UCN are filled. Within this cylinder is an adjustable plate with an absorber attached. This plate is adjusted to different heights corresponding to different gravitational potentials. The gravitational potential (E_{grav}) of the UCN takes the form:

$$E_{\mathrm{grav}} = m_{\mathrm{n}} g h = 1.0252 \left[\frac{\mathrm{neV}}{\mathrm{cm}}\right] \times h[\mathrm{cm}], \tag{4.1}$$

where m_{n} is the mass of the neutron, g is the gravitational constant, and h is the change in height of the neutron. Given Eqn. 1.7 the UCN produced in the source at RCNP must move through a potential of 102.52 neV in order to reach the top plate of the gravity spectrometer at its maximum height of 1 m. For the vertical UCN source the walls of the production vessel are coated with ^{58}Ni which has a Fermi potential of 212.96 neV. Therefore, any UCN produced in the source with an energy higher than this will escape from the production volume. After production, the UCN must move upward and travel through a gravitational potential of approximately 100 neV. Therefore, the UCN which reach the spectrum bottle have kinetic energies between approximately 0 and 112 neV. Upon reaching the PE plate inside the cylinder the UCN are absorbed. However, only UCN with a sufficiently large kinetic energy can reach the top plate. The energy required to reach the absorbing plate is a function of the plate height. For example, given the plate at a height of 40 cm, the maximum kinetic energy an UCN can have without interacting with the absorber plate is 41.0 neV. Most UCN with energy higher than this will be absorbed in the top plate of the gravity spectrometer and only UCN with energies lower than this maximum energy has a chance to reach the detector to be counted.

The configuration of the UCN guides and gravity spectrometer at RCNP for this spectrum measurement can be found in Fig. 4.1. The full (a)-(f) sequence of a spectrum measurement is performed as follows, with (a)-(d) matching the steps shown in Fig. 4.2:

(a) The UCN are produced in the source volume for a period of 60 s, with both the filling and emptying valves of the spectrum bottle closed.

(b) After this production period the filling valve is opened and the UCN move into the main cylindrical volume, for a period of 20 s. The emptying valve remains closed.

(c) After the filling period the filling valve on spectrum bottle is closed again. The UCN are stored for a delay time Δt. During this time UCN with a high enough energy have a chance of reaching the absorbing plate and being absorbed. UCN without sufficient energy to reach

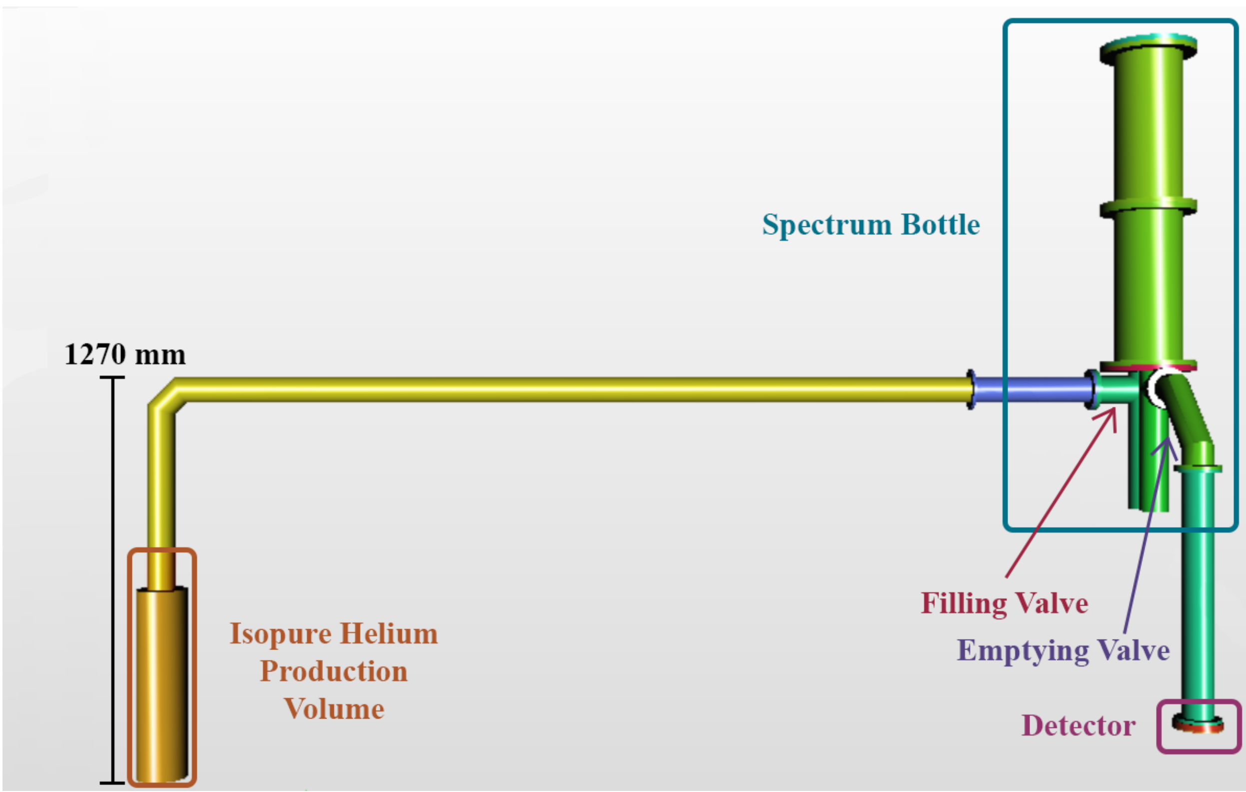

Figure 4.1: Model of the UCN guides in the RCNP setup including the spectrum bottle. The simulated UCN were initialized in an isopure Helium volume outlined in orange with the filling valve closed. The spectrum bottle and detector are labelled in blue and red, respectively.

the absorbing plate will interact only with the stainless steel walls and therefore will be stored for longer times.

(d) After the delay time, the emptying valve of the cylinder is opened and the remaining UCN move out of the volume and towards the detector where they are counted.

(e) In order the determine the storage lifetime of the gravity spectrometer with the plate at a given height the above sequence is repeated with various Δt from 0 s to 500 s. The Δt is then tuned for the specific plate height to maximize statistics.

(f) In order to measure the energy spectrum, the plate is adjusted to different heights and the above steps are repeated. The experiments performed at RCNP used plate heights between 5 cm and 84.5 cm [31].

The RCNP spectrum experiments were performed with only one ^{3}He detector. The total counts were normalized to the proton beam during the production period.

The inner diameter of the spectrum bottle is 206 mm and the total height is 1000 mm, which is composed of two joined 50 cm cylinders. The adjustable plate is shown in Fig. 4.3 which presents a model of the gravity spectrometer. The bottom of the plate is made of Polyethylene (PE), which is assumed to be a black UCN absorber.

In order to extract the energy spectrum from these measurements the counts ($f(\Delta t)$) as a function of time from the time delays listed in the above steps are first fit to a double exponential decay of the form:

$$f(t) = A_1 e^{-t/\tau_1} + A_2 e^{-t/\tau_2}. \tag{4.2}$$

τ_1 and τ_2 are free parameters for the fit representing the long and short lifetimes of the decay. A_1 and A_2 are free parameters for the fit corresponding to the initial number of UCN produced. It is important to note that in this case the τ_2 and A_2 have been chosen to correspond to the long

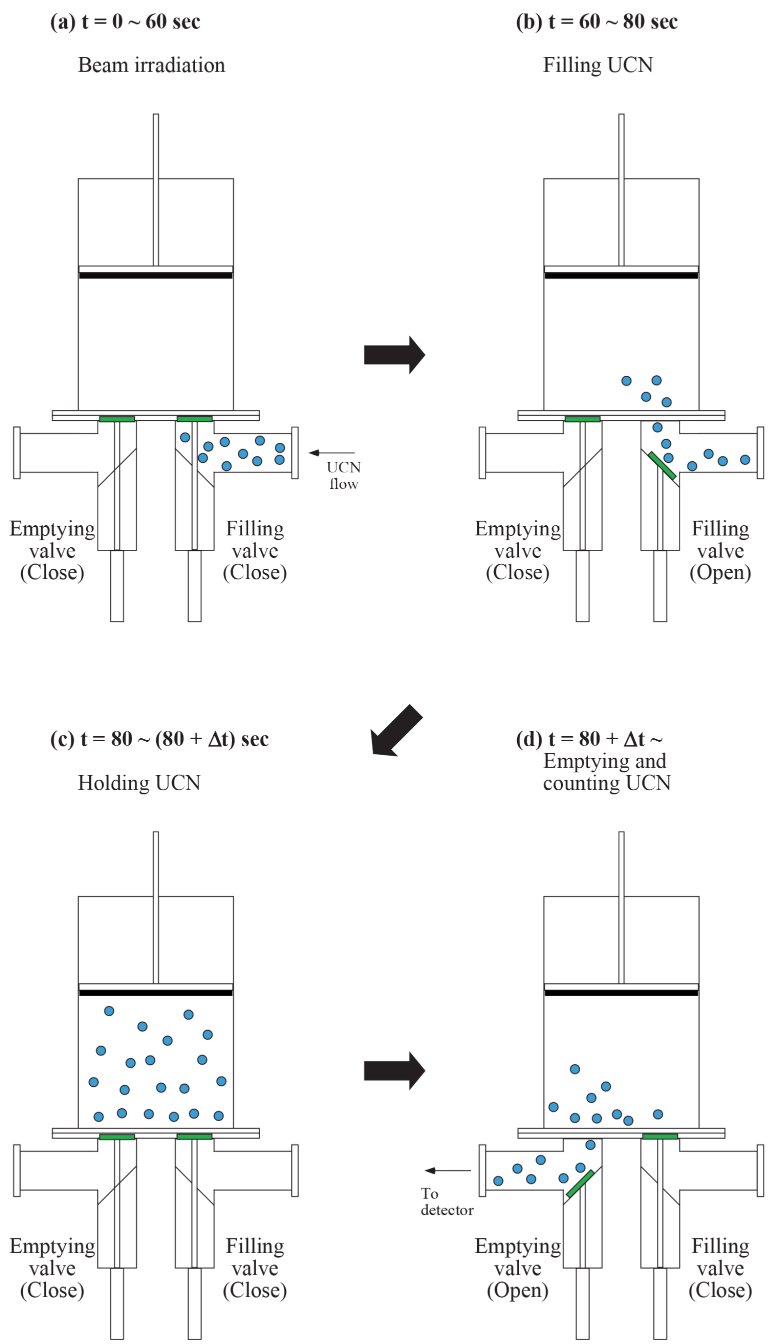

Figure 4.2: A simplified schematic of the gravity spectrometer through the measurement steps. The steps (a)-(d) of the sequence for production, filling, storage, emptying, and measurement in the RCNP spectrum bottle are shown. The UCN absorber is shown in black. The UCN are depicted with blue circles, the filling and emptying valves are depicted in green [31]. See the text for a description of the steps.

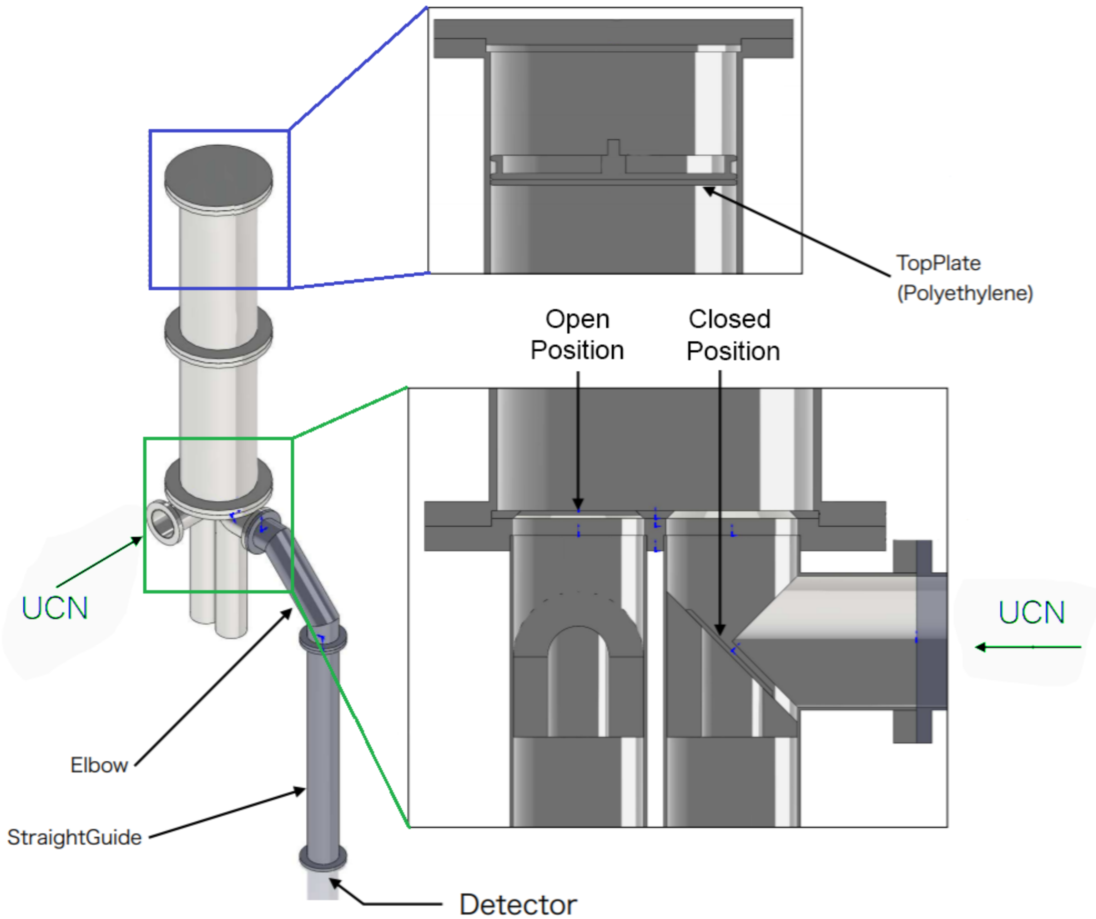

Figure 4.3: The model of the RCNP gravity spectrometer used in simulations with labels on the significant components. On the left it is shown where the UCN should enter the bottle, filling via the valve on the right in the insert (in the closed position), indicated by an arrow. They are stored in the cylinder for some period with both valves closed. Finally, the UCN are emptied via the valve on the left in the insert (in the open position). The Top Plate component is adjusted to various heights throughout the simulation. Everything not otherwise labelled is stainless steel [31].

component of the decay, which is the slower UCN, by setting the starting value for τ_2 as higher than τ_1. For a UCN energy spectrum $\rho(E)$ the magnitude of the long component is described by

$$A_2 = \int_0^{m_{\mathrm{n}}gh} \rho(E)dE. \tag{4.3}$$

Therefore, by differentiating Eqn. 4.3 one can obtain the UCN energy spectrum.

4.1.2 Simulations of the RCNP Setup and Comparison to Data

The first simulations of the RCNP setup were done using the Fermi potentials for stainless steel (SS) that have been determined from simulations and measurements at TRIUMF. It was found that the lifetimes of the RCNP source simulated in PENTrack were far longer than those measured at RCNP.

The source volume is the same as in the simulations done for TCN18-020 and TCN18-021, using a NiP surface. The production time is 60 s. UCN are produced with a square root energy spectrum between 0 and 300 neV. The rest of the components are modeled as stainless steel, apart from the polyethylene plate. The polyethylene material in the simulation has a real Fermi potential of -8.6553 neV, and an imaginary potential of 0.492 neV.

The timing of the valves is as follows. The filling valve and the emptying valve begin in the closed state for the simulation and remain as such for the 60 s production period. In the simulation a brief delay of 2 s follows this production period to model the delay of the valve opening. The filling valve then remains open for 20 s, allowing the UCN to move into the spectrum bottle. After this filling time, the valve closes again and the UCN are stored for between 2-500 s. Then the emptying valve is open and the UCN can move towards the detector.

It was also found that the double exponential of Eqn.4.2 was a poor fit for the simulated data. The double exponential fits were giving nonphysical results for the majority of the plate heights, although it did work for the 40 cm position. However, the discrepancies in the storage lifetime trends were well illustrated by a single exponential fit, and the same analysis to find the Fermi potential can be performed with the single exponential fit. For the following analysis the fits for both the simulated and measured data being discussed are single exponential fits of the form:

$$f(t) = A_1 e^{-t/\tau_1}. \tag{4.4}$$

The preliminary approach of addressing the difference in the storage lifetime observed in simulations is the modification of the material properties of the guides and gravity spectrometer, namely the Fermi potential of the SS, which is one of the primary factors impacting the storage lifetime of the gravity spectrometer.

A benchmark configuration must be chosen in order to determine an approximate value for the Fermi potential of the gravity spectrometer's inner cylinder as input to the simulations. In order to tune this Fermi potential, the absorbing plate in the gravity spectrometer was set to 40 cm height. A set of simulations were then performed, scanning through the possible Fermi values for the SS until a lifetime matching the lifetime of the RCNP gravity spectrometer was found. The SS imaginary Fermi potentials of 0.8, 0.6, 0.4, 0.2, 0.16, and 0.10 neV were simulated. With an imaginary Fermi potential of 0.16 neV, a double exponential fit of the simulated storage lifetime for the 40 cm position resulted in $\tau_1 = 40 \pm 20$ s and $\tau_2 = 177 \pm 5$ s. This agrees within uncertainty with the data from RCNP with $\tau_1 = 30 \pm 20$ s and $\tau_2 = 180 \pm 10$ s. This value for the SS Fermi potential was used to simulate the other plate positions and the lifetimes were compared. The real part of the potential was left unmodified.

Plate Height	**Simulated τ**	**χ^2 / DOF**	**Measured τ**	**χ^2/DOF**
10	289 ± 7	2.04	121 ± 9	2.64
20	234 ± 8	0.74	120 ± 7	4.42
30	190 ± 4	0.66	135 ± 5	3.90
40	167 ± 3	1.13	153 ± 5	2.51
50	156 ± 2	1.09	159 ± 5	1.49
80	127 ± 1	0.67	163 ± 4	0.67

Table 4.1: A table of parameters from the simulated and measured lifetimes from the gravity spectrometer fit with a single exponential. It can be seen that the simulated and measured lifetimes trend in different directions over the range of plate heights. Additionally, the spread of the simulated lifetimes is much larger than that of the measured lifetimes.

A summary of the fitted lifetimes of simulated and measured data is shown in Tab. 4.1, corresponding to the graphs in Fig. 4.4 and Fig. 4.5. The lifetimes agree for the heights close to the 40 cm position, but do not match as well for the very high and very low plate positions. As a reflection of this it is important to compare the relative goodness of the fits for the lifetime, as this might shed some light on why the lifetimes are matched differently for different heights. The quality of the fits, determined by the χ^2/DOF, decreased in both the simulation and the experiments for the lower plate heights. The storage lifetime from simulated data decreased as the plate was raised, shown in Fig. 4.4. In this figure the counts in the absorber are normalized to the total number of UCN simulated. The fit parameter A_1 is not shown as it is not relevant to this aspect of the analysis. The storage lifetime from the measured data increased as the plate was raised, shown in Fig. 4.5. The reversal of the expected trend in the storage lifetime exposes a significant discrepancy between the data and simulation.

For comparison of the data taken at RCNP and the simulation data it was important to use the same fitting method. The data from RCNP was put into the same ROOT fitting scheme as the simulation data, which involved a single exponential fit over similar time delays. A comparison of the simulation lifetime and the data taken at RCNP showed two clear distinct trends. As discussed above, the SS imaginary Fermi potential was determined in an analysis which compared double exponential fits of simulated and measured data. In this analysis, the same simulated data

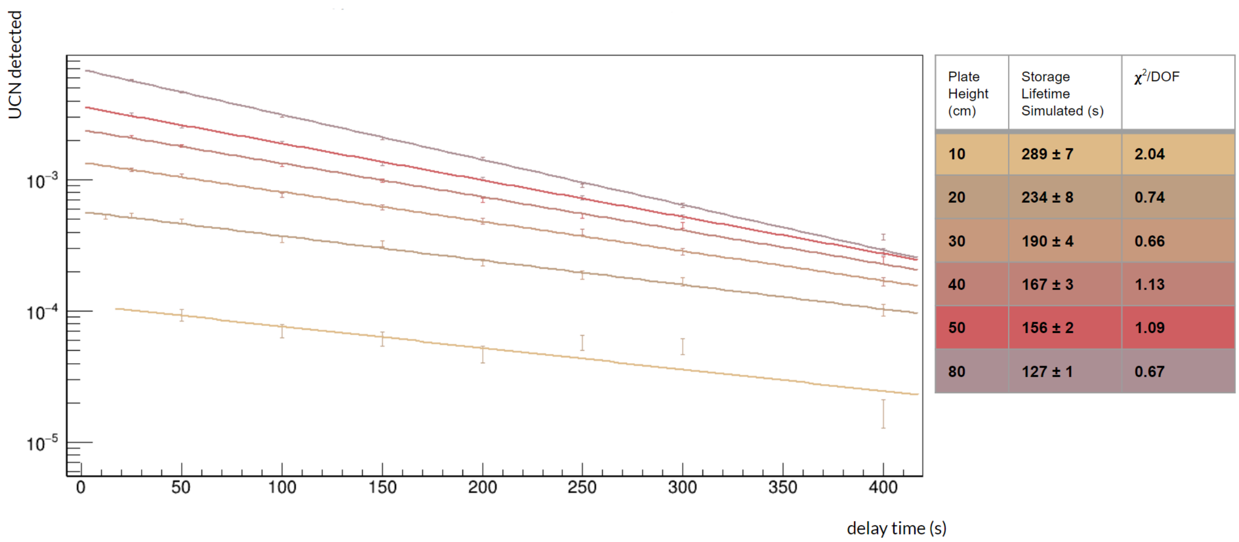

Figure 4.4: Lifetimes for a simulated spectrum of the RCNP source from plate heights 10 to 80 cm, fit with a single exponential. The fits for the plate heights are coded with the colors from the legend on the right. The y-axis is the number of detected UCN over the number of simulated UCN. The points plotted are the simulated data. As the height of the plate was raised, the storage lifetime of the spectrum bottle decreased.

was fit to a single exponential. For the analysis done in [31] most of the storage lifetimes were fit with a double exponential. Therefore, it was necessary to refit most of the data taken at RCNP. The delays and plate heights which were considered from RCNP were chosen to match the ones that were simulated. The change in plate height from 10 to 80 cm in the simulations resulted in a change in storage lifetime of 162 ± 8 s. This is a significantly larger change than the change in storage lifetime of 42 ± 13 s for the data taken at RCNP. The difference in both the direction and the scale of the trend implies that the interactions of the UCN with the material of the spectrum bottle is modeled incorrectly.

Ultimately there appears to be a significant difference in the energy dependent behavior between simulation and experiment. Specifically, it seems that in the simulations far more of the fast UCN are lost throughout the runtime than in the experiment, resulting in a longer storage lifetime as the plate is lowered and all that remains are the slow UCN. With a single exponential fit on the

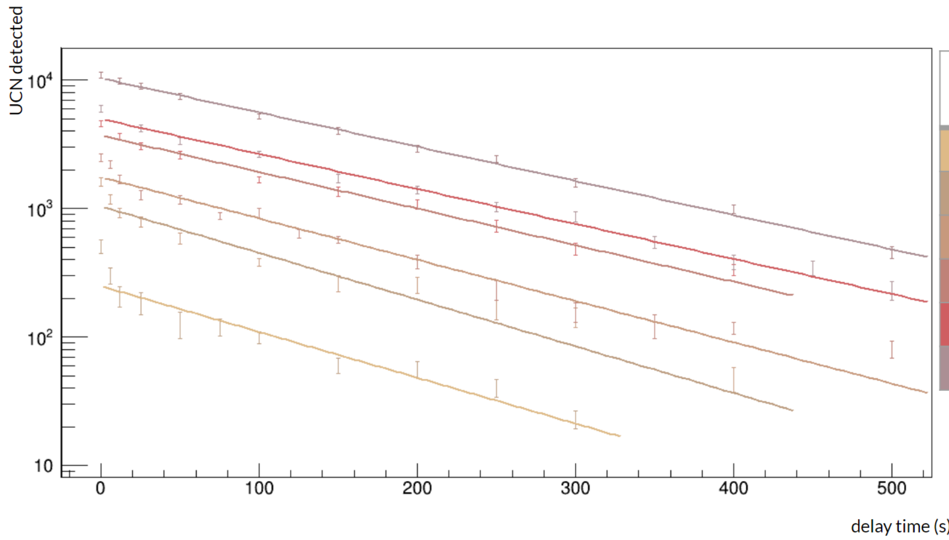

Plate Height (cm)	Storage Lifetime (s)	χ^2/DOF
10	121 ± 9	2.64
20	120 ± 7	4.42
30	135 ± 5	3.90
40	153 ± 5	2.51
50	159 ± 5	1.49
80	163 ± 4	0.67

Figure 4.5: Lifetimes for the measured spectrum of the RCNP source from plate heights 10 to 80 cm, fit with a single exponential. The fits for the plate heights are coded with the colors from the legend on the right. The y-axis is the UCN counts in the detector normalized the beam current during irradiation. The points plotted are the measured data. As the height of the plate was raised, the storage lifetime of the spectrum bottle increases.

simulated storage lifetime the lifetime of the spectrum bottle started relatively low at 127 ± 1 s for the 80 cm position. The lifetimes steadily increase as the plate was lowered, ultimately reaching 289 ± 7 s for the 10 cm height. The experimental data resulted in a storage lifetime of 163 ± 4 s for the 80 cm position. This lifetime steadily decreased as the plate was lowered, and reached 121 ± 9 s at 10 cm. There is a clear difference in range and direction of trends between the simulation and experiment. There are several potential explanations for this difference.

One is that the model of the PE makes it a significantly better UCN absorber in simulations than it is in reality. An incorrectly modeled PE plate would result in the absorption of more UCN over the course of the storage in the simulations than would be absorbed in reality. Potential future work would be investigating the change in the storage lifetimes with a change in Fermi potential of the PE. Additionally, one could match simulations to experiments done with the same spectrum bottle with no PE plate, just the bare SS. Both approaches could reveal potential reasons for this difference in storage lifetime.

Alternatively, the differences may be due to a fundamental assumption made about the interactions of UCN with surfaces. The most recent update of the PENTrack simulation software includes an experimental parameter which defines the wall losses of UCN to be energy independent and instead each interaction corresponds to a pre-set loss-per-bounce probability which is constant across the energy spectrum. This modification also has the potential to fix the discrepancies observed between simulations and experiment. This is the most likely explanation, as several other experiments performed within the TUCAN collaboration have shown similar discrepancies between the measured value and the simulation [48] [39].

CHAPTER 5

CONCLUSION

In conclusion the work of this thesis has contributed to the detailed understanding of the UCN prototype source currently installed at TRIUMF. Two main aspects were investigated in this thesis, the determination of the relative responses of two UCN detectors used at the TRIUMF UCN facility and investigations of the UCN energy spectrum produced with the UCN prototype source at RCNP. For both investigations, data analyses as well as simulations have been performed, constituting an important benchmarking of the simulation framework.

UCN detectors usually rely on the combination of an energy dependent absorption process of neutral neutrons resulting in an excited nucleus and subsequent decays into charged particles. These charged particles are then detected with the standard methods of charge amplification in gas or scintillation. Currently TUCAN uses a ^{6}Li scintillating glass detector and a ^{3}He gas proportional counter. Through an analysis of detection rates for UCN produced and directed to the ^{6}Li or ^{3}He detectors in alternating batches, a ratio of the relative responses can be determined. The UCN are directed to one detector at a time using a rotary valve. The process of the analysis involved the compensation for potential transport asymmetries in the rotary valve, and the investigation of possible background effects or UCN source performance instabilities due to effects from fluctuating source parameters such as the cryostat temperature or proton beam current. The relative response of the ^{3}He to ^{6}Li detector was found to be $65.2 \pm 0.1\%$.

A subsequent simulation of the rotary valve and the two detectors revealed the simulated detection efficiency ratio was $80.7 \pm 0.4\%$. Therefore it is necessary to scale the counts in the simulated ^{3}He detector by 80.9% in order reflect the experimental findings accordingly in subsequent simulations. The simulated efficiency of the ^{3}He detector was adjusted because the ^{6}Li detector model is more detailed and deemed closer to reality. This factor is used to increase the accuracy of UCN simulations of transmission and storage experiments before comparing to data. The accuracy of PENTrack is very important because it is used to estimate the performance of the planned future upgrade of the TRIUMF UCN facility.

In addition to the detector analysis, analysis work on the proton current directed onto the UCN spallation target was performed. The total accumulated proton beam intensity on the spallation target for the 2018 UCN measurement campaign was evaluated. This process was based on the analysis of the previous run in 2017, however modifications of the analysis were required to take into account changes in the electronics of beam diagnostics elements. Finally, the current predicted by beamline operational settings was compared to measurements in a torodial non-intercepting monitor (TNIM). This monitor is part of the machine protection system of the proton beam line and cyclotron. A cross verification of its accuracy is important to ensure it is performing as expected. For the currents relevant for the monitor to trigger on, TNIM2 correlates well with the predicted current. The total integrated beam on target for 2018 was 65.6 ± 0.1 μAh.

The investigations of the UCN energy spectrum produced with the vertical UCN source prototype cryostat included the following objectives: reproducing the measured energy spectrum taken in 2013 at the Research Center for Nuclear Physics at Osaka (RCNP) via simulations and estimate the measurement time required to achieve significant statistics if a spectrum measurement were to be repeated at TRIUMF. As the source currently being used at TRIUMF has been characterized in great detail at RCNP, one could assume that the energy spectrum that it produced is the same as was measured at RCNP. However, the surface of the UCN production volume might have deteriorated during transport. In addition, the total UCN guide length between source and experiment is not the same, and different qualities of guides were used in certain portions. These changes could potentially affect the observable energy spectrum. Thus, it has been determined important to use the same spectrometer to repeat the energy spectrum measurement at TRIUMF. During the preparatory simulations performed to gauge the time requirements for a spectrum measurement it was discovered that PENTrack simulations of the spectrum bottle produced un-physical results. The simulated spectrum had an inverted trend for the storage lifetime for the different spectrometer setups from the analyzed experimental data taken at RCNP. Several potential explanations for this discrepancy were presented along with future routes of investigation which resulted in changes to the simulation software. This is important because PENTrack is used to model all UCN experiments at TRIUMF.

Additional work done for the TUCAN collaboration can be found in Appendix A, which describes the comparison of smooth vs jointed UCN elbows, to determine the scale of the benefit that smooth guides can have.

The work presented in this thesis aids in the development of the future UCN source at TRIUMF. It quantified the relative responses of the two available detectors, the total beam on target for the 2018 run, the correlation of the two beam current measurement devices, and presented a discrepancy in the simulation software. This work will aid in the development of the future UCN source, quantifying various tools and properties used to perform several experiments, in order to ultimately allow for the high precision search of the electric dipole moment of the neutron, which could shed light on the mystery of baryon asymmetry in the universe.

Appendices

APPENDIX A

COMPARISON OF TRANSMISSION EFFICIENCIES OF SMOOTH VS JOINTED UCN GUIDE ELBOWS

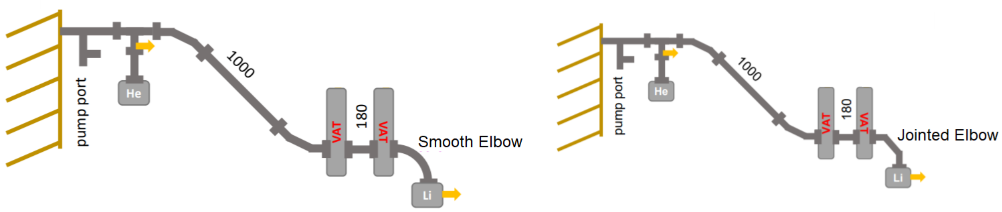

Figure A.1: Configurations for the smooth and jointed elbow transmission experiments. On the left the configuration has a smooth elbow connecting the last valve to the UCN detector. On the right is the same configuration, but with a jointed elbow. The lengths of the guides are given in black. The two valves are labelled as VAT.

This analysis will be a part of making an informed decision about the difference in cost to transport efficiency of a smooth vs jointed bend. There are several angled joints within the UCN setup. This could potentially improve the final UCN count in the detector.

The transmission rates of the two configurations over several cycles is shown in Fig. A.2. The transmission rate is taken to be the average of the rates within the cycles. The transmission rate of the smooth elbow is $16.97 \pm 0.07\%$. The transmission rate of the jointed elbow is $11.58 \pm 0.06\%$. The averages of the transmitted UCNs over several cycles during each run shows that the smooth elbow has a slightly higher transmission than that of the jointed elbow by $5.4 \pm 0.1\%$. This implies that the smooth elbows would be more ideal to use in the TUCAN experiment. Ultimately, the improvement in the transmission efficiency from the smooth elbows must be weighted against the cost of manufacture. In this case, the expense of manufacturing smooth elbows for the whole setup

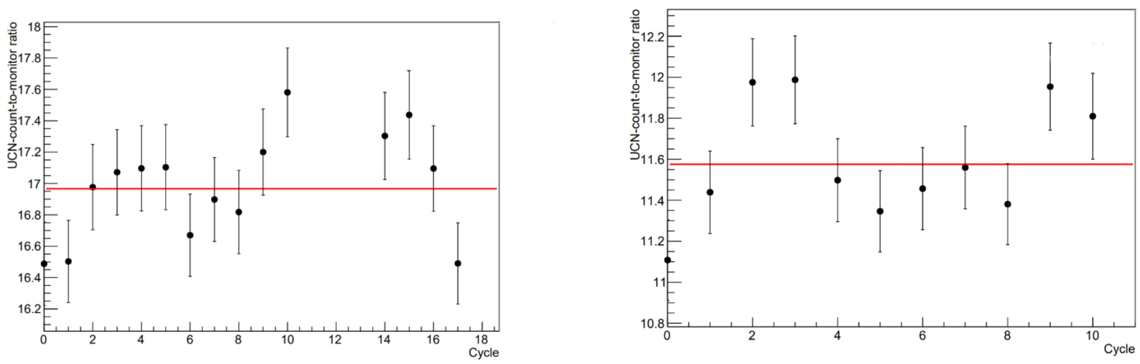

Figure A.2: Transmission rates of smooth and jointed elbows, as represented by the ratio of the monitor counts to measured counts. On the right is the transmission rate for the jointed elbow. On the left is the transition rate for the smooth elbow.

may be better spent on other improvements to the source, as the increase in transmission efficiency is relatively small.

REFERENCES

[1] L.Canetti, M,Drewes, M.Shaposhnikov, "Matter and Antimatter in the Universe," *New Journal Phys.*, vol. 14, p. 095 012, Nov. 2012. DOI: 10.1088/1367-2630/14/9/095012.

[2] A.D. Sakharov, "Violation of CP Invariance, C Asymmetry, and Baryon Asymmetry of the Universe," *Sovi. Journal of Expe. Theo. Phys. Letters*, vol. 5, pp. 392–393, 1967. DOI: 10.1070/PU1991v034n05ABEH002497.

[3] S. Bertolini, A. Maiezza, F. Nesti, "Kaon CP violation and neutron EDM in the minimal left-right symmetric model," *Phys. Review D*, vol. 101, p. 034 502, Feb. 2020. DOI: 10.1103/PhysRevD.101.035036.

[4] A. R. Maxim Pospelov, "Electric dipole moments as probes of new physics," *Annals Phys.*, vol. 318, pp. 119–169, Feb. 2008. DOI: 10.1016/j.aop.2005.04.002.

[5] J.M. Pendlebury et all, "Revised experimental upper limit on the electric dipole moment of the neutron," *Phys. Review D*, vol. 92, p. 092 003, 2015. DOI: 10.1103/PhysRevD.92.092003.

[6] A. P. Serebrov, E. A. Kolomenskiy, A. N. Pirozhkov, et all, "New search for the neutron electric dipole moment with ultracold neutrons at ILL," *Phys. Review C*, vol. 92, p. 055 501, 2015. DOI: 10.1103/PhysRevC.92.055501.

[7] C. Abel, S. Afach, N.J. Ayres, "Measurement of the permanent electric dipole moment of the neutron," *Phys. Letters A*, vol. 124, p. 081 803, Feb. 2020. DOI: 10.1103/PhysRevLett.124.081803.

[8] A. P. Serebrov, E. A. Kolomenskiy, A. N. Pirozhkov, et all, "Measurement of the neutron lifetime using a magneto-gravitational trap and in situ detection," *Science*, vol. 11, pp. 627–632, 2018. DOI: 10.1126/science.aan8895.

[9] A. P. Serebrov, E. A. Kolomensky, A. K. Fomin, et all, "Neutron lifetime measurements with a large gravitational trap for ultracold neutrons," *Phys. Review C*, vol. 97, p. 201 805, 2018. DOI: 10.1103/PhysRevC.97.055503.

[10] M. P. Mendenhall, et all, "Precision measurement of the neutron Beta-decay asymmetry," *Phys. Review C*, vol. 87, pp. 808–810, 2013. DOI: 10.1103/PhysRevC.87.032501.

[11] H. Abele, T. Jenke, D. Stadler, et all, “QuBounce: the dynamics of ultra-cold neutrons falling in the gravity potential of the Earth,” *Nucl. Phys. A*, vol. 827, 2009. DOI: 10.1016/j.nuclphysa.2009.05.131.

[12] Y. Masuda, K. Hatanaka, S. Jeong, “Spallation Ultracold Neutron Source of Superfluid Helium below 1 K,” *Phys. Review Letters*, vol. 108, p. 108, Mar. 2012. DOI: 10.1103/PhysRevLett.108.134801.

[13] L. W. Alvarez, F. Bloch, “A quantitative determination of the neutron magnetic moment in absolute nuclear magnetons,” *Phys. Review*, vol. 57, pp. 111–122, 1940. DOI: 10.1103/physrev.57.111.

[14] A. Knecht, “Towards a new measurement of the neutron electric dipole moment,” PhD thesis, Universität Zürich, 2009.

[15] M. Tegmark, et al, “Cosmological parameters from SDSS and WMAP,” *Phys. Review D*, vol. 69, 2004. DOI: 10.1103/PhysRevD.69.103501.

[16] D. N. Spergel, L. Verde, H. V. Peiris, et al, “First Year Wilkinson Microwave Anisotropy Probe (WMAP) Observations: Determination of Cosmological Parameters,” *Astrophys. Journal Supplement*, vol. 148, p. 200 405, 2003. DOI: 10.1086/377226.

[17] TUCAN Collaboration, “Status Update on the Next Generation UCN Source at TRIUMF and the Proton Beamline 1U,” 2019.

[18] E. Fermi, W. N. Zinn, “Phase of Neutron Scattering,” *Phys. Review*, vol. 70, 1946.

[19] R. Golub, D. Richardson, S.K. Lamoreaux, *Ultra-Cold Neutrons*. CRC Press: Taylor and Francis Group, 1991.

[20] E. Fermi and L. Marshall, “Interference Phenomena of Slow Neutrons,” *Phys. Review*, vol. 71, pp. 666–677, 10 May 1947. DOI: 10.1103/PhysRev.71.666.

[21] K. Bodek, M. Daum, R. Henneck, “Storage of ultracold neutrons in high resistivity, non-magnetic materials with high Fermi potential,” *Nucl. Inst. Meth. Phys. A*, vol. 597, pp. 222–226, Oct. 2008. DOI: 10.1016/j.nima.2008.09.018.

[22] A. Steyerl, H. Nagel, F. -X Schreiber, et all, “A new source of cold and ultracold neutrons,” *Phys. Letters A*, vol. 116, pp. 347–352, 1986. DOI: 10.1016/0375-9601(86)90587-6.

[23] E. Korobkina, R. Golub, B.W. Whring,A.R. Young, “Production of UCN by downscattering in superfluid He4,” *Phys. Letters A*, vol. 301, pp. 462–469, Sep. 2002. DOI: 10.1016/S0375-9601(02)01052-6.

[24] T. M. Ito, et all, “Performance of the upgraded ultracold neutron source at Los Alamos National Laboratory and its implication for a possible neutron electric dipole moment experiment,” *Phys. Review C*, vol. 97, p. 201 801, 2018. DOI: 10.1103/PhysRevC.97.012501.

[25] H. J. Maris, “Phonon-phonon interactions in liquid helium,” *Review Modern Phys.*, vol. 49, 2 Apr. 1977. DOI: 10.1103/RevModPhys.49.341.

[26] R. Golub, J.M. Pendlebury, “The Interaction of Ultra-Cold Neutrons (UCN) with Liquid Helium and a Superthemal UCN Source,” *Phys. Letters*, vol. 62A, pp. 337–339, Sep. 1977. DOI: 10.1016/0375-9601(77)90434-0.

[27] O.Zimmer, F.M. Piegsa, S.N. Ivanov, “Superthermal Source of Ultracold Neutrons for Fundamental Physics Experiments,” *Phys. Rev. Letter*, vol. 107, p. 201 109, 2011. DOI: 10.1103/PhysRevLett.107.134801.

[28] A.P. Serebrov, V.A. Mityuklyaev, A.A. Zakharov, “Preparation of facilities for fundamental research with ultracold neutrons at PNPI,” 2019.

[29] M.R. Gibbs, W.G. Stirling, “Temperature Dependence of the Phonon-Maxon Excitations in Superfluid 4He at SVP and 20 Bars,” *Journal Low Temp. Phys.*, vol. 102, p. 249, 1996. DOI: 10.1007/BF00754661.

[30] M. R. Gibbs, K. H. Anderson W.G. Stirling, “The collective excitations of normal and superfluid 4He: the dependence on pressure and temperature,” *Journal Phys.: Cond. Matter*, vol. 11, pp. 603–628, 1999. DOI: S0953-8984(99)97081-9.

[31] R. Matsumiya, “Study of He-II Spallation UCN Source,” PhD thesis, Osaka University, 2013. DOI: 10.18910/26156.

[32] *PENTrack Github*. [Online]. Available: github.com/wschreyer/PENTrack.

[33] W. Schreyer, T. Kikawa, M. J. Losekamm, S. Paul, R. Picker, “PENTrack—a simulation tool for ultracold neutrons, protons, and electrons in complex electromagnetic fields and geometries,” *Nucl. Inst. Meth. Phys.*, vol. 858, pp. 123–129, Oct. 2016. DOI: 10.1016/j.nima.2017.03.036.

[34] F. Atchison, M. Daum, R. Henneck, et all, “Diffuse reflection of ultracold neutrons from low-roughness surfaces,” *Euro. Phys. Journal A*, vol. 44, pp. 23–29, 2010. DOI: 10.1140/epja/i2010-10926-x.

[35] F. Pedrotti, L. Pedrotti, *Introduction to Optics*. Pearson Prentice Hall, 2007.

[36] F. Atchison, M, Daum, R. Henneck, “Diffuse Reflection of Ultracold Neutrons from Low-Roughness Surfaces,” *Euro. Phys. Journal A*, vol. 44, pp. 23–29, Mar. 2010. DOI: 10.1140/epja/i2010-10926-x.

[37] S. Wlokka, P. Fierlinger, A. Frei, et all, “Consistent description of UCN transport properties,” 2017.

[38] V. Bargmann, L. Michel, and V. L. Telegdi, “Precession of the Polarization of Particles Moving in a Homogeneous Electromagnetic Field,” *Phys. Review Letters*, vol. 2, pp. 435–436, 10 May 1959. DOI: 10.1103/PhysRevLett.2.435.

[39] *Private Communication: New PENTrack features from meeting*.

[40] J. Dilling, R. Krucken, L. Merminga, *isac and ariel : The triumf radioactive beam facilities and the scientific program*.

[41] S. Ahmed, T. Andalib, M.J. Barnes, “A beamline for fundamental neutron physics at TRIUMF,” *Nucl. Inst. Meth. Phys. Research A*, vol. 927, pp. 101–108, May 2019. DOI: 10.1016/j.nima.2019.01.074.

[42] L. Lee, “UCN Beamline at TRIUMF BL1U Overview and Installation Status,” 2016.

[43] *Ucn kicker diagnostics and control*.

[44] N. Ramsey, “A Molecular Beam Resonance Method with Separated Oscillating Fields,” *Phys. Review*, vol. 78, pp. 695–699, Jun. 1950. DOI: 10.1103/PhysRev.78.695.

[45] J. M. Pendlebury, W. Heil, Yu. Sobolev, P. G. Harris, et all, “Geometric-phase-induced false electric dipole moment signals for particles in traps,” *Phys. Review A*, vol. 70, p. 20 040 901, 2004. DOI: 10.1103/PhysRevA.70.032102.

[46] B. Franke, “Investigations of the Internal and External Magnetic Fields of the Neutron Electric Dipole Moment Experiment at the Paul Scherrer Institute,” PhD thesis, ETH ZÜRICH, 2013.

[47] TUCAN Collaboration, “Conceptual Design Report for the Neutron Electric Dipole Moment Spectrometer at TRIUMF,” 2020.

[48] S. Sidhu, “Improving the sensitivity of the neutron electric dipole moment experiment at TRIUMF,” CAP2019, 2019. [Online]. Available: https://indico.cern.ch/event/776181/contributions/3353461/.

[49] A. Ahmed, E. Altiere, T. Andalib, “First ultracold neutrons produced at TRIUMF,” *Phys. Review C*, vol. 99, p. 025 503, Feb. 2019. DOI: 10.1103/PhysRevC.99.025503.

[50] B. Jamieson, L.A. Rebenitsch, S. Hasen-Romu, “Characterization of a scintillating lithium glass ultra-cold neutron detector,” *Euro. Phys. Journal A*, vol. 53, p. 201 701, Jan. 2017. DOI: 10.1140/epja/i2017-12195-7.

[51] A.V. Strelkob, *Private Communication: Dunia-10 Spec Sheet.*

[52] S. Imajo, K. Mishima, M. Kitaguchi, “Pulsed ultra-cold neutron production using a Doppler shifter at J-PARC,” *Prog. Theor. Exp. Phys.*, Jan. 2016. DOI: 10.1093/ptep/ptv177.

[53] *Short notes about UCN gaseous detector(type Dunia-10, made in FLNP, JINR).*

[54] CERN, *ROOT a Data Analysis Framework*. [Online]. Available: https://root.cern.ch/.

[55] J. R. Clement, J. K. Logan, and J. Gaffney, “Liquid Helium Vapor Pressure Equation,” *Phys. Review*, vol. 100, pp. 743–744, 2 Oct. 1955. DOI: 10.1103/PhysRev.100.743.

[56] R. Webber, “A Tutorial on Non-Intercepting Electromagnetic Monitors for Charged Particle Beams,” 2017.

[57] F. Atchison, B. Blau, A. Bollhalder, et all, “Transmission of very slow neutrons through material foils and its influence on the design of ultracold neutron sources,” *Nucl. Inst. Meth. Phys. Research A*, vol. 608, pp. 144–151, 2009. DOI: 10.1016/j.nima.2009.06.047.